



저작자표시-비영리-변경금지 2.0 대한민국

이용자는 아래의 조건을 따르는 경우에 한하여 자유롭게

- 이 저작물을 복제, 배포, 전송, 전시, 공연 및 방송할 수 있습니다.

다음과 같은 조건을 따라야 합니다:



저작자표시. 귀하는 원저작자를 표시하여야 합니다.



비영리. 귀하는 이 저작물을 영리 목적으로 이용할 수 없습니다.



변경금지. 귀하는 이 저작물을 개작, 변형 또는 가공할 수 없습니다.

- 귀하는, 이 저작물의 재이용이나 배포의 경우, 이 저작물에 적용된 이용허락조건을 명확하게 나타내어야 합니다.
- 저작권자로부터 별도의 허가를 받으면 이러한 조건들은 적용되지 않습니다.

저작권법에 따른 이용자의 권리는 위의 내용에 의하여 영향을 받지 않습니다.

이것은 [이용허락규약\(Legal Code\)](#)을 이해하기 쉽게 요약한 것입니다.

[Disclaimer](#)

공학박사 학위논문

**Development of Micrometer Resolution
Dosimetry using Radiochromic Film by
Raman Spectroscopy and its Application to
Measuring the Radioenhancement of Gold
Nanofilm**

라만분광법과 방사선감광필름을 이용한 마이크로미터
해상도 방사선량 측정법 개발 및 금나노필름에 의한
방사선량 증가 측정에서의 응용

2018년 8월

서울대학교 융합과학기술대학원

융합과학부 방사선융합의생명전공

Jamal Ahmad Mirza

A Dissertation for the Degree Doctor of Philosophy

**Development of Micrometer Resolution
Dosimetry using Radiochromic Film by
Raman Spectroscopy and its Application to
Measuring the Radioenhancement of Gold
Nanofilm**

라만분광법과 방사선감광필름을 이용한 마이크로미터
해상도 방사선량 측정법 개발 및 금나노필름에 의한
방사선량 증가 측정에서의 응용

August 2018

Program in Biomedical Radiation Sciences
Department of Transdisciplinary Studies
Graduate School of Convergence Science and Technology
Seoul National University

Jamal Ahmad Mirza

Abstract

Development of Micrometer Resolution Dosimetry using Radiochromic Film by Raman Spectroscopy and its Application to Measuring the Radioenhancement of Gold Nanofilm

Jamal Ahmad Mirza

Program in Biomedical Radiation Sciences

Department of Transdisciplinary Studies

Graduate School of Convergence Science and Technology

Seoul National University

Purpose: Due to increasing demand for high-spatial resolution dosimetry, radiochromic films (RCFs) have been investigated as a potential candidate, but are often limited by the scanning system, e.g., flatbed optical scanner. Micrometer resolution dosimeters are necessary to evaluate the doses in

regions with high dose gradients in brachytherapy, radiosurgery, measuring the peak to valley dose ratios in synchrotron microbeam radiotherapy, and assessing dose enhancement by metal nanoparticles. In this study, Raman spectroscopy in conjunction with a microscope was selected as an alternative method for high-spatial resolution dosimetry of RCF. We also investigated the possibility of using confocal Raman spectroscopy to quantify the radiation dose with micrometer spatial resolution on RCF. Finally, we applied this technique to quantitatively measure the radiation dose enhancement due to photon interactions with gold nanoparticles (GNPs).

Method: The commercial RCFs, EBT3 and EBT-XD were irradiated with known doses using 50, 100, 200 and 300 kVp, and 6 MV X-rays. Dose levels from 0.3 to 30 Gy were chosen for this work. The confocal Raman spectroscopy was used to quantify the dose on the films by applying the Raman mapping technique in a region of interest (ROI) of $100 \times 100 \mu\text{m}^2$ with a spatial resolution of 10 μm . An achievable spatial resolution, clinically useful dose range, dosimetric sensitivity, dose uniformity, an effect of orientation, energy and dose rate dependence, and post-irradiation stability of both types of RCFs were characterized with a micrometer resolution.

The developed technique was applied to measure the radiation dose enhancement. Gold nanofilms (GNFs) of nominal thicknesses 20, 30, 40, 50, and 100 nm were prepared by evaporating pure gold on polyethylene terephthalate (PET) substrate. The GNF can be considered as a large cluster of GNPs. The GNF attached to RCF was irradiated using 50 and 220 kVp, and 6 MV flattening filter free (FFF) X-rays. The active layer of the RCF touched the gold-coating of GNF, while the uncoated PET substrate faced the X-ray

source. The radiation doses to the active layer of the RCF with and without GNF were measured using an optical flatbed scanner and confocal Raman spectrometer. The ratio of the doses with and without GNF was defined as the dose enhancement factor (DEF). In addition, the analytical calculation of the DEF was carried out with an aid of Monte Carlo simulations.

Results: Due to partial diacetylene polymerization upon irradiation, two Raman peaks of C=C and C≡C stretching bands were observed around 1447 cm^{-1} and 2060 cm^{-1} , respectively. Data acquired in an ROI of $100 \times 100 \mu\text{m}^2$ with a spatial resolution of 10 μm showed dose non-uniformity of <10%. The EBT-XD film was less sensitive than the EBT3 film. The dose-response with the peak ratio of C≡C stretching and C-C-C deformation bands at 2058 cm^{-1} and 696 cm^{-1} respectively was also measured. The peak ratio method reduced the dose non-uniformity at micrometer level into ~3%. The C≡C band height response for both RCF types measured in the landscape orientation was more sensitive than those in the portrait orientation for all dose levels. The EBT3 and EBT-XD films showed weak energy dependency. Both RCFs were independent of dose rates and have a stable response after 24-hour post-irradiation. EBT3 films were suitable for low dose range of 0 to 6 Gy whereas, EBT-XD films were more suitable for high dose range of 2 to 20 Gy.

The dose enhancement factors measured by an optical scanner ranged from 2.13 (± 0.33) to 6.11 (± 0.38) at 50 kVp and 1.63 (± 0.59) to 4.88 (± 0.36) at 220 kVp for 20 to 100 nm thick GNFs. Similarly, the DEFs measured by Raman spectroscopy ranged from 2.55 (± 0.59) to 4.60 (± 1.04) at 50 kVp and 2.21 (± 0.53) to 4.76 (± 0.82) at 220 kVp for the same films. The analytically calculated DEFs ranged from 2.04 to 6.16 at 50 kVp and from 1.74 to 4.86 at

220 kVp, as the thickness of GNF increased from 20 to 100 nm. However, there was almost no dose enhancement estimated by both measured methods and analytical calculation for high-energy X-ray. The analytical DEFs were in agreement with the measured values. In general, the radioenhancement increases with increasing the thickness of GNF, while it decreases with increasing the energy of X-rays.

Conclusions: The Raman intensity for C=C and C≡C peaks increases with increasing radiation doses due to the increasing amount of diacetylene polymerization. This study showed the potential of Raman spectroscopy as an alternative for absolute dosimetry verifications with a high-spatial resolution of a few μm . The Raman dosimetry developed in this study needs to be further validated for the purpose of microdosimetry. Both EBT3 and EBT-XD films were suitable for micrometer resolution dosimetry when read out by confocal Raman spectroscopy. Results of dosimetric characterization suggest that EBT3 films were suitable for low dose range of 0 to 6 Gy whereas, EBT-XD films were more suitable for high dose range of 2 to 20 Gy. Lastly the dose enhancement due to low-energy X-ray interactions with GNPs was quantitatively validated by measuring the variations in optical densities and Raman spectral shift on the RCFs. The experimental and analytical approaches developed in this study would be useful to quantitatively estimate radiosensitization of high-Z metallic nanoparticles by low-energy X-rays, which has been an emerging interest in diagnostic and therapeutic applications of nanoparticles. This work has a limitation in self-absorption and backscattering of low-energy electrons where the characteristics of GNF may differ from those of GNPs in tissues. In future, Raman spectroscopic

dosimetry will be extended to achieve a micrometer resolution with greater dose uniformity by using two-peak ratio method. New polymer materials need to be explored as a potential candidate for Raman dosimetry.

Keywords: Micrometer resolution dosimetry, Raman spectroscopy, Confocal, high-spatial resolution, radiochromic film, Gold nanoparticle and film, Radioenhancement

Student Number: 2014-31483

List of Tables

- Table 1. Principal Raman vibrational bands of monomer, partial polymer and monomer free polymer.^{a 48} 35
- Table 2. Mean, standard deviation (SD), and relative standard deviation (RSD) from measured Raman mapping data of 121 pixels of C≡C peaks around 2060 cm⁻¹ for region of interest of 100 × 100 μm² with spatial resolution of 10 μm at radiation doses ranging from 0 to 30 Gy for both types of radiochromic films (for 6 MV X-rays). These values were calculated after applying preprocessing steps to all peaks..... 48
- Table 3. Mean, standard deviation (SD), and relative standard deviation (RSD) for C-C deformation peak (Peak 1), C≡C stretching peak (Peak 2) and their ratio (Peak 2 / Peak 1). Peak ratio method has least variation but less sensitive than C≡C peak method. The data is acquired with 150 grooves/mm grating..... 51
- Table 4. Student *t*-test for EBT3 film. The lowered tailed independent two sample *t*-test on consecutive dose maps in a region where error bars start overlapping in Figure 16(a). Significance level = 0.05, null hypothesis: mean I – mean II ≥ 0, and alternative hypothesis: mean I – mean < 0..... 53
- Table 5. Student *t*-test for EBT-XD film. The lowered tailed independent two sample *t*-test on consecutive dose maps in a region where error bars start overlapping in Figure 16(a). Significance level = 0.05, null hypothesis: mean I – mean II ≥ 0, and alternative hypothesis: mean I – mean < 0.. 54
- Table 6. Orientation response ratio for quantification of effect of film orientation when readout by Raman spectroscopy..... 57
- Table 7. Energy response ratios for type EBT-3 film to compute the energy dependence of various kVp X-rays relative to 6 MV X-rays. 60
- Table 8. Energy response ratios for EBT-XD film to compute the energy dependence of various kVp X-rays relative to 6 MV X-rays. 61
- Table 9. Dose rate response ratios of radiochromic films to observe the dose rate dependence of two different types of radiochromic films. 64
- Table 10. Post-irradiation response ratio of radiochromic films w.r.t. stable dose readings taken after one week. 67
- Table 11. Density and fractional weight composition of PET and EBT-XD films.⁴².. 84
- Table 12. Coating thicknesses of Gold nanofilms (GNFs) measured by Alpha-Step and their respective densities⁸⁵ and masses. Fractions of electrons entering into the active layer of radiochromic film from GNF calculated by the

MCNP 6.1 code are also included in the table.....	92
Table 13. List of DEFs for 50 and 220 kVp, and 6 MV FFF X-rays for GNFs of various thicknesses. These values were estimated by three different methods i.e. optical scanner, Raman spectrometer and analytical approach with an aid of MC simulations.	99

List of Figures

Figure 1. Polymerization of diacetylene monomers by photons. ³²	12
Figure 2. Film structure and dimensions: (a) Unlaminated and (b) Laminated EBT3 Film and (c) EBT-XD film. ³⁹	13
Figure 3. Active particles (chromophores) in (a) EBT3 films and (b) EBT-XD films. ³⁸	14
Figure 4. Pinhole aperture spatially filters the (a) horizontal and (b) vertical out-of-focus rays. ⁵² (c) Pinhole aperture installed with Raman spectroscopy system at Seoul National University. ⁵³	18
Figure 5. Confocal image of USAF target standard of group 9 elements 2, 3, 4, 5, and 6 (a) with pinhole size of 30 μm and (b) without pinhole. The image size is $30 \times 30 \mu\text{m}^2$ with spatial resolution of 300 nm. The objective lens used was Olympus 100 \times magnification. Thickness of dashes for element 1, 2, 3, 4, 5, and 6 are 976.6, 870, 775.1, 690, 615.2, and 548.1 nm, respectively. ⁵³	20
Figure 6. Illustration of spherical aberration of lens of focal length f when trying to focus the laser at a distance Δ below the ample surface. The surface refraction shifts the focus deeper into the sample at distance $n\Delta$. The depth resolution (DR) increase linearly with Δ . ⁴¹	23
Figure 7. Depth profile through 4 layer polymer laminate using (Upper) 100 \times oil immersion objective and (Lower) 100 \times metallurgical objective. ⁴¹	25
Figure 8. Line spread function (LSF) and edge spread function. A mathematical relationship exists between ESF and LSF. Fourier transform of LSF gives the spatial resolution of an imaging system. ⁶¹	28
Figure 9. The limiting spatial resolution is the spatial frequency at which the amplitude of the modulation transfer function (MTF) decreases to some agreed-upon level. Here the limiting spatial resolution is shown at 10% modulation, and the limiting spatial resolution is 1.6 cycles/mm. ⁶¹	29
Figure 10. Schematic diagram of active layer of EBT-XD after irradiation. $1 \times 1 \text{ cm}^2$ GNF with thicknesses 50 and 100 nm were fabricated such that left half of each film was PET only and right half was PET coated with GNF. The GNF was then attached with the active layer of $3 \times 3 \text{ cm}^2$ unlaminated EBT-XD film.	31
Figure 11. Fourier transform Raman spectra of (a) monomer, (b) partial polymer and (c) monomer free polymer (excitation wavelength is 1064 nm). ⁴⁸	34
Figure 12. (a) Changes in the relative intensities of 2220 cm^{-1} ($\nu\text{C} \equiv \text{C}$ of monomer) and 2123 cm^{-1} ($\nu\text{C} \equiv \text{C}$ of polymer) bands as a function of γ -ray dosage in the partial polymer: (i) 0 Mrad; (ii) 18 Mrad (iii) 59 Mrad; (iv) 84 Mrad; (v)	

140 Mrad; (vi) 100% polymer. (b) Plot of relative intensities of the 2123 cm^{-1} band with respect to the 2220 cm^{-1} band as a function of γ -ray dosage in the partial polymer (relative intensity = ratio of polymer peak height to monomer peak height multiplied by 10).⁴⁸ 36

Figure 13. Raman spectrum of radiochromic film.³² The peak 1 at 696 cm^{-1} corresponds to a C-C-C deformation peak whereas the peak 2 at 2058 cm^{-1} belongs to the C \equiv C peak. 38

Figure 14. The Raman spectrum of active layer of a radiochromic film (EBT-XD) irradiated with a dose of 1 Gy. The centers of prominent peaks are noted above the peaks. 43

Figure 15. (a) and (b) shows the edge spread functions (ESFs) for the GNFs of thicknesses 50 and 100 nm, respectively. Black solid line represents the original horizontal profile when scanning with step of 10 μm is done from no gold area to gold coated area (10 \times 2000 μm). (c) and (d) presents the modulation transfer functions (MTFs) for (a) and (b) respectively. The spatial resolution at 10% modulation is (a) 0.01849 cycles/ μm and (b) 0.01999 cycles/ μm , which is equivalent to (a) \sim 54 μm and (b) \sim 50 μm 45

Figure 16. (a) Dose calibration curves with band heights of carbon triple bond (0-30 Gy, 6 MV X-rays). Each black square and red circle represent data point of EBT3 and EBT-XD radiochromic film, respectively. Error bars indicate one standard deviation of the mean of 121 pixels at region of interest of 100 \times 100 μm^2 on each film with spatial resolution of 10 μm . EBT3 and EBT-XD curves are fitted by an exponential functions of two components with R-squared values of 0.9987 and 0.9985 respectively. The solid lines represent fitted curves. (b) For comparison, the fitted curves of both types of radiochromic films as shown in Figure 16(a) are normalized from 0 to 1. It can be inferred that EBT3 is more sensitive than EBT-XD but saturates earlier. 47

Figure 17. Dose response with respect to (a) C \equiv C band height and (b) ratio of C \equiv C stretching band peak height to C-C-C deformation band peak height. Dose response with C \equiv C band height is more sensitive than that of Peak ratio method, however, the standard deviation is \sim 3% in case of Peak ratio dose response. 50

Figure 18. Normalized dose response of (a) EBT3 and (b) EBT-XD film with different orientation. In case of both radiochromic film types, the films measured with landscape orientation have higher sensitivity than that with portrait orientation. The curves are normalized to the average values of C \equiv C band height of landscape orientation at 30 Gy. 56

Figure 19. Variation of Carbon triple bond band heights with dose to observe the energy dependence for (a) EBT3 film and (b) EBT-XD film. Error bars

indicate one standard deviation of the mean of 121 pixels at region of interest of $100 \times 100 \mu\text{m}^2$ on each film with spatial resolution of $10 \mu\text{m}$. . 59

Figure 20. Variation of Carbon triple bond band heights with dose to observe the dose rate dependence for (a) EBT3 film, and (b) EBT-XD film, when irradiated at 200 kVp X-rays. Error bars indicate one standard deviation of the mean of 121 pixels at region of interest of $100 \times 100 \mu\text{m}^2$ on each film with spatial resolution of $10 \mu\text{m}$ 63

Figure 21. Change of the carbon triple bond band heights as a function of time since irradiation for EBT3 and EBT-XD films exposed to 0.5 Gy and 2 Gy at 200 kVp. Error bars indicate one standard deviation of the mean of 121 pixels at region of interest of $100 \times 100 \mu\text{m}^2$ on each film with spatial resolution of $10 \mu\text{m}$ 66

Figure 22. Schematic of GNF and unlaminated EBT-XD film irradiated by X-rays (not scaled). On the active layer of the unlaminated EBT-XD film, GNF and PET without gold were irradiated by X-ray beams. PET without gold was used as a control to calculate DEF. Beneath this geometry 5 cm solid water was placed for backscatter. For 6 MV FFF beam, a 5 cm build-up phantom was additionally placed on the top of this geometry..... 79

Figure 23. Schematic diagram of irradiation configurations for analytical calculation of dose enhancement (not scaled): (a) When gold nanoparticles (GNPs) of total mass mAu are uniformly mixed with radiochromic film, low-energy electrons (LEEs) will deposit the whole energy into the radiochromic film. (b) The actual experimental setup in which the gold nanofilm (GNF) is attached to the active layer of radiochromic film. Polyester base of radiochromic film and PET substrate of GNF is not shown in the figure. . 87

Figure 24. Gold nanofilms of various coating thicknesses on PET substrate. The thicknesses denoted here are nominal values. 91

Figure 25. Dose calibration curves of (a) an optical scanner (error bars are the same size or smaller than the symbols) (b) and a Raman spectrometer for 50, 220 kVp, and 6 MV FFF..... 94

Figure 26. Arrays of unlaminated EBT-XD films after irradiation of 50, 220 kVp, and 6 MV FFF under GNF. X-axis indicates delivered doses 0, 0.3, 0.5, 1.0, and 1.5 Gy. Y-axis indicates the thicknesses of GNFs 0, 20, 30, 40, 50, and 100 nm. Darker color means that the EBT-XD film was more irradiated (along x-axis) or more dose-enhanced (along y-axis). The color became darker with increasing the thickness of GNF at (a) 50 kVp and (b) 220 kVp beams. However, the dose enhancement by change of thickness was hardly seen from the films irradiated by (c) 6 MV FFF beam. 96

Figure 27. Comparison of DEF obtained from optical scanner, Raman spectroscopy, and analytical calculations for photon energies of (a) 50 kVp, (b) 220 kVp, and (c) 6 MV FFF beam. For low-energy X-rays DEF was an increasing

function of GNF thickness, whereas enhancement was negligible for high-energy X-rays. 98

Contents

Abstract	i
List of Tables	vi
List of Figures	viii
General Introduction.....	3
1. Micrometer Resolution Dosimetry using Radiochromic Film by Raman Spectroscopy	6
1.1. Introduction	6
1.2. Methods and Materials	9
1.2.1. Films and Irradiation	9
1.2.2. Resonance Raman Spectroscopy	15
1.2.3. Confocal Raman Micro-Spectroscopy.....	17
1.2.3.1. Spatial Resolution of Confocal Raman Microscopy.....	19
1.2.3.1.1. Lateral Spatial Resolution	19
1.2.3.1.2. Axial Spatial Resolution.....	21
1.2.3.2. Metallurgical vs Oil Immersion Objective.....	22
1.2.4. Data Acquisition and Analysis.....	26
1.2.4.1. Raman Mapping	26
1.2.4.2. Spatial Resolution.....	27
1.2.4.3. Calibration Curves, Dose Ranges and Dosimetric Sensitivity	32
1.2.4.3.1. Calibration Curves using C≡C Band Heights	32
1.2.4.3.2. Calibration Curves using Peak Ratio.....	32
1.2.4.4. Dose Uniformity	39
1.2.4.5. Effect of Orientation of Radiochromic Films	39
1.2.4.6. Energy and Dose Rate Dependence	40
1.2.4.7. Post-Irradiation Stability.....	41
1.3. Results	42
1.3.1. Assignment of Raman Peaks of Active Layer of Radiochromic Film	42
1.3.2. Spatial Resolution.....	44
1.3.3. Dose Calibration and Dosimetric Sensitivity.....	46
1.3.4. Dose Range.....	52
1.3.5. Dose Uniformity	55
1.3.6. Effect of Radiochromic Film Orientation	55
1.3.7. Energy Dependence	58
1.3.8. Dose Rate Dependence	62
1.3.9. Post-Irradiation Stability.....	65

1.4.	Discussion	68
1.5.	Conclusions	73
2.	Application of Raman Spectroscopy to Measuring the Radioenhancement of Gold Nanofilm.....	74
2.1.	Introduction	74
2.2.	Methods and Materials	76
2.2.1.	Preparation of Gold Nanofilm	76
2.2.2.	Preparation of RCF Samples	77
2.2.3.	Sample Irradiation and Calibration.....	77
2.2.4.	Radiochromic Film Reading.....	80
2.2.4.1.	Optical Flatbed Scanner.....	80
2.2.4.2.	Raman Spectroscopy	81
2.2.5.	Macroscopic Dose Enhancement Factor.....	82
2.2.6.	Analytical Approach	83
2.2.6.1.	Analytical Macroscopic Dose Enhancement Factor	83
2.2.6.2.	Monte Carlo Simulations for Estimating fFwd	89
2.3.	Results	90
2.3.1.	Thickness Measurements of GNF	90
2.3.2.	Calibration Curves.....	93
2.3.3.	Dose Enhancement Factor	95
2.3.3.1.	Experimental Measurement	95
2.3.3.2.	Analytical Approach	100
2.4.	Discussion	102
2.5.	Conclusions	104
	Discussion	105
	Conclusions and Future work.....	107
	References	109
	Appendix A.	118
	Abstract (in Korean).....	119

General Introduction

For the last two decades, there has been a substantial advance in cancer treatment by radiation, such as intensity modulated radiation therapy, volumetric modulated arc therapy, and stereotactic ablative radiotherapy.¹⁻³ Newly developed radiological imaging and therapy instruments have improved the tumor localization and management. Brachytherapy sources can generate a steep dose gradient between the tumor and adjacent healthy tissue. In radiobiology, we need to know about spatial, temporal and spectral distributions of energy imparted in cellular and subcellular structures and the associated biological effects.⁴ Space industry has a requirement to study the effect of ionization radiation on microelectronic devices intended for space use.⁵ All of the above mentioned innovative devices and scientific industries require dose evaluation in regions with high gradients, at buildup and interface regions. Conventional radiation detectors, like an ionization chamber or a semiconductor detector, have certain limitations, such as a relatively large sensitive volume or non-water equivalence. Other unsuitable dosimeters include thermoluminescent detectors due to the time-consuming readout procedure and inability to archive their dosimetric data and radiographic films that are non-water equivalent, sensitive to light and require wet chemical processing.⁶ On the other hand, polymer gels and radiochromic films (RCFs) have been considered suitable for these clinical needs because of their high spatial resolution and near water equivalence.⁷ Recently, the use of metal nanoparticles has become increasingly popular in medical imaging, drug

delivery, and radiation therapy applications, which require dosimeters capable of measuring dose enhancement at the cellular and even subcellular level.⁸

The micrometer resolution dosimeters proposed in past few decades require continual refinement. It is possible to take real-time dose measurements with metal oxide semiconductor field-effect transistor (MOSFET) or Silicon diodes and fiber-optic dosimeters. A spatial resolution of less than 1 μm is conceivable with MOSFET based devices (Bräuer-Krisch et al.⁹, Siegbahn et al.¹⁰); however such devices show energy dependency due to an atomic number greater than Z_{eff} of water or tissue. M. D. Belley et al.¹¹ developed a dosimetry measurement technique using a nanoparticle-terminated fiber-optic dosimeter and demonstrate a resolution of 100 μm , but calibration is an issue because of non-water equivalency. Recently, James Archer et al.¹² constructed a water equivalent fiber-optic dosimeter using plastic scintillator having the same resolution.

Polymer gels and RCFs are not real-time detectors. Despite this drawback, they have a high spatial resolution, water equivalency, and accuracy. Simon J. Doran et al.¹³ achieved a spatial resolution of 40 μm by scanning radiochromic polymer PRESAGE™ gels with optical computed tomography. J. C. Crosbie et al.¹⁴ measured the spatial resolution of Gafchromic™ HD-810 films as 25 μm , using a microdensitometer. Guerda Massillon-JL et al.¹⁵ reported a spatial resolution of 85 μm with large uncertainties during the study of a dosimetry system consisting of Gafchromic™ EBT3 film and a flatbed optical scanner. Recently, we at Seoul National University selected a Raman spectroscopy in conjunction with a microscope as an alternative

method for high spatial resolution dosimetry of RCF and developed a novel Raman mapping technique to studying the variation in Raman spectra of C=C and C≡C (carbon double bond and carbon triple bond) stretching bands of diacetylene polymer as a function of therapeutic X-ray doses.¹⁶

The advent of nanotechnology has given a new dimension to the diagnostic and therapeutic management of cancer.¹⁷⁻²¹ Promising results from early in vivo and in vitro experiments confirmed that the metal nanoparticles (NPs) have great potential to maximize the therapeutic effect of radiotherapy.²²⁻²⁸ The developed Raman spectroscopic dosimetry was also applied to measuring the radioenhancement of gold nanofilm with micrometer resolution. The so-called “radioenhancement” can be explained by the phenomenon that low-energy photons (below a hundred keV) have large peak cross-sections of photoelectric interaction on K- and L-shells of high-Z materials (e.g., ⁷⁹Au- / ⁶⁴Gd-NPs). Atomic reorganization after these photoelectric interactions leads to the emission of a large number of low-energy electrons (LEE) i.e., photoelectrons, Auger electrons and Coster-Kronig electrons.²⁹ Assuming the loading of metal NPs to tumors, these LEEs following the photoelectric interactions penetrate into the surrounding tumorous tissue and result in a significantly increased energy deposition within a few tens nanometer ranges from the metal NPs.

The research objectives include the characterization of EBT3 and EBT-XD radiochromic film dosimeters at micrometer resolution by confocal Raman spectroscopy and application of Raman spectroscopy to measuring the radioenhancement of gold nanofilms (GNFs).

Chapter I

1. Micrometer Resolution Dosimetry using Radiochromic Film by Raman Spectroscopy

1.1. Introduction

Radiochromic film dosimeters are considered suitable for micrometer resolution dosimetry due to its high intrinsic spatial resolution, low energy dependence, dose rate independence, and near-water equivalence.^{30,31} The active layer of Gafchromic™ EBT series RCFs (Ashland Specialty Ingredients, Bridge Water, NJ) consists of diacetylene monomers in an ordered form, which on the application of UV light or high-energy radiation are polymerized and progressively darkens with increased radiation exposure.³¹⁻³³ Traditionally dose quantification of exposed RCF is assessed by the linear absorbance measurement using a flatbed-scanner or a densitometer.³⁴ Flatbed-scanner equipped with white light is widely used for dose estimation and a densitometer with low power laser is used for high spatial resolution dosimetry. Recently, we suggested a Raman spectroscopy in conjunction with a microscope as an alternative method for high spatial resolution dosimetry of RCF.¹⁶ It is always good to have new readout devices for film dosimetry as every device has some limitations. The modulation transfer function (MTF) of the flatbed scanning system is not adequate to provide high spatial resolution dose profile.³⁵ On the other hand, a densitometer can be used as a high spatial

resolution dosimeter but with high dose variations. However, reading out with Raman spectroscopy is advantageous in a sense that dose variation is about 3% when data is acquired with micrometer spatial resolution. With Raman spectroscopy, we can detect any delicate chemical changes caused by radiation. Moreover, with Raman spectroscopy, we can analyze polymerization in colorless polymers. The document scanner or densitometer cannot analyze colorless films. Also, at low doses, the calibration curves obtained by Raman microscopy are more sensitive than document scanner or densitometer.

In film dosimetry, it is possible to attain micrometer resolution, if intrinsic spatial resolutions of the dosimeter, as well as readout capability of the instrument, are in micrometers. According to Christopher G Soares, the chromophores (needle-like particles) with a diameter of 0.75 μm in the active layer of RCFs can be considered as the absolute limit of film resolution.^{34,36} Likewise, depending on the laser wavelength, the microscope objective and confocal pinholes used during Raman spectroscopy, a spatial resolution of less than 1 μm is possible.³⁷ The purpose of this work was to measure the quantity of radiation dose in sites comparable to sizes of living cells as small as 10 μm using EBT3 and EBT-XD RCFs (Ashland Specialty Ingredients, Bridge Water, NJ), by confocal Raman micro-spectroscopy.³⁸⁻⁴⁰ Confocal Raman micro-spectroscopy is advantageous for chemical and material analysis with increased lateral resolution, and non-destructive analysis of a transparent sample at a certain depth.⁴¹ We characterized the new EBT-XD film dosimeter, with the comparison to EBT3. We compared the clinically useful dose range, dosimetric sensitivity, dose uniformity, effect of orientation,

energy and dose rate dependence, and post-irradiation stability of both RCF types. To our knowledge, there is no published data describing radiation dose on Gafchromic EBT3 and EBT-XD films with a spatial resolution of 10 μm by Raman micro-spectroscopy.

1.2. Methods and Materials

1.2.1. Films and Irradiation

Measurements were performed with RCF model EBT3 (Lot #06061601) and EBT-XD (Lot #12101501). A radiochromic film (RCF) is a chemical dosimeter that changes its color after radiation exposure.³⁴ These materials integrate absorbed dose information and require a readout procedure to generate this information. RCFs are suitable for the absorbed doses delivered in external beam therapy and brachytherapy. The Gafchromic films by Ashland Specialty Ingredients, Bridge Water, NJ, USA are widely used for radiotherapy.³¹ Their latest versions, the EBT3 and EBT-XD, were used in this study because of their capability of measuring therapeutic doses with high-resolution two-dimensional spatial information.³⁹ Moreover, these RCFs are near tissue-equivalent and less energy dependent.³⁴ Unlike radiographic film, RCF does not require chemical processing.

The active layer of Gafchromic™ RCF consists of lithium salt of pentacosanoic, 12-diyonic acid (LiPCDA) monomers in ordered form, which on application of UV light or high-energy radiation are polymerized (see also Figure 1), darkening with increasing exposure.³¹ Figure 2 shows the schematic diagrams of EBT3 and EBT-XD radiochromic films used in this work.³⁹ The EBT-3 film is comprised of an about 28 μm thick active layer, constituting of the active component with marker dye.³⁹ The active layer is packed in between two 125 μm matte polyester substrates.^{39,40} The EBT-XD film has the same structure as the EBT3 film except an active layer is about 25 μm and somewhat different chemical composition.³⁹ The size and shape of

chromophores in both film types are different. The lengths of chromophores are 15 to 20 μm and 2 to 4 μm in EBT3 and EBT-XD films, respectively whereas; the diameters of chromophores are 1 to 2 μm for both film types (see Figure 3).⁴⁰ EBT-XD is specifically designed for high radiation doses.⁴² Films were stored below 25°C, handled carefully to avoid unwanted exposure to radiation and sunlight and gloves were worn to avoid fingerprints distorting the measurements.³¹

Traditionally dose quantification of exposed RCF is assessed by the linear absorbance measurement.³⁴ Flatbed-scanner equipped with white light is widely used for dose estimation. A densitometer with low power laser is used for high spatial resolution dosimetry.³⁴ Recently, we at Seoul National University selected a Raman spectroscopy in conjunction with a microscope as an alternative method for high-spatial resolution dosimetry of RCF.¹⁶

A document scanner is a low-cost approach to read RCF.³⁴ It is equipped with a white light source and can acquire images in both transmission and reflection modes.⁴³ The acquired image is usually stored in 48 bit TIFF format. The image is then converted into separate color components using commercially available software like ImageJ (National Institutes of Health, Bethesda, MD, USA).^{44,45} The red channel is usually used for dose evaluation. The modulation transfer function (MTF) of the system is not adequate to provide high spatial resolution dose profile.³⁵ A densitometer with low power lasers, such as He/Ne and the diode lasers or a broadband red-light emitting source is used for high-resolution dosimetry. The MTF of a typical device, ESRF, a Joyce Loebel microdensitometer, estimates a spatial resolution of

about 25 μm . Densitometer lacks reproducibility and is sensitive to individual adjustment.^{14,35}

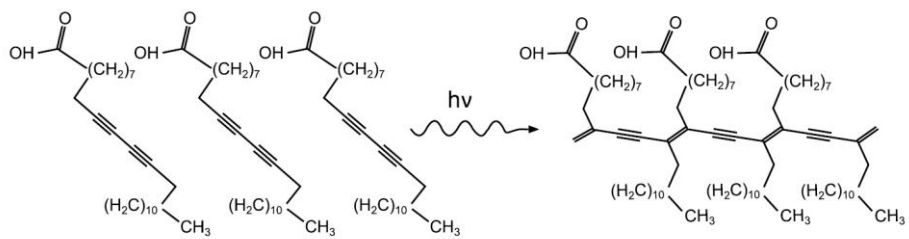
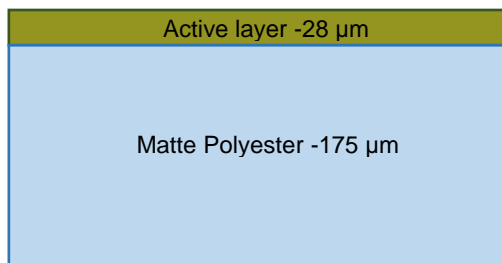
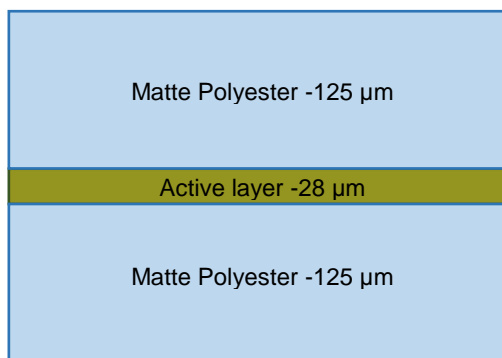


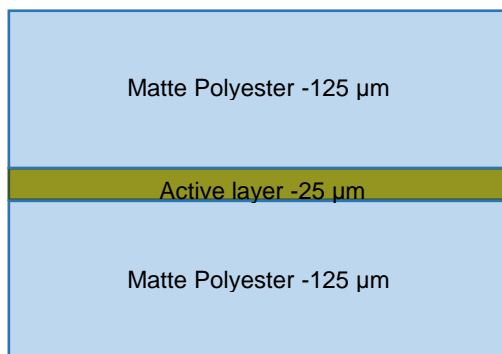
Figure 1. Polymerization of diacetylene monomers by photons.³²



(a)



(b)



(c)

Figure 2. Film structure and dimensions: (a) Unlaminated and (b) Laminated EBT3 Film and (c) EBT-XD film.³⁹

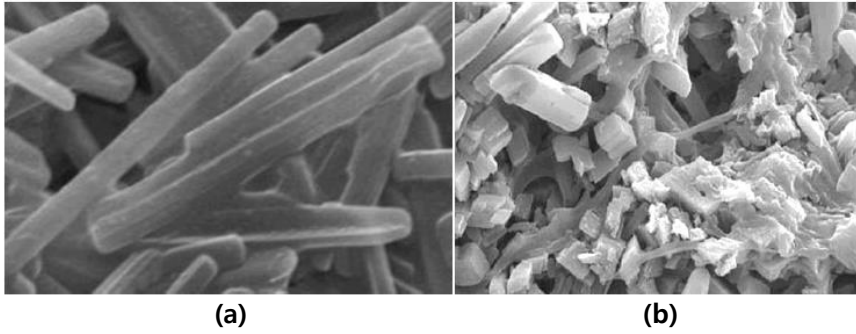


Figure 3. Active particles (chromophores) in (a) EBT3 films and (b) EBT-XD films.³⁸

The film sheets were cut into $2 \times 2 \text{ cm}^2$ pieces, and each piece was marked with an arrow on the right corner to indicate orientation.⁴⁶ These pieces were irradiated using a clinical linear accelerator (Trilogy Varian System, Palo Alto, CA) at Seoul National University Hospital with $10 \times 10 \text{ cm}^2$ field of 6 MV beam. The films were sandwiched between a 5 cm solid water slab at the bottom and a 1 cm bolus material and 0.5 cm solid water slab on the top, such that the films were placed at the point of maximum dose on the central axis. The films were exposed to 0.3, 0.5, 1, 2, 4, 6, 8, 10, 15, 20, and 30 Gy at a source-to-surface distance (SSD) of 100 cm.

To check the energy and dose rate dependence, and post-irradiation development with time of both types of film dosimeters; we irradiated the films with kVp X-rays (50, 100, 200, and 300 kVp) using X-RAD 320 Biological Irradiator (Precision X-Ray, Inc., N. Branford, CT). The films were exposed to 0.3 to 6 Gy in-air for 50 kVp X-rays and in-phantom at a depth of maximum dose of 2 cm for the rest of the kVp X-rays at an SSD of 50 cm, as per TG 61 recommendations.⁴⁷

1.2.2. Resonance Raman Spectroscopy

Raman spectroscopy has been widely used to study the electronic and vibrational structure of polymers.⁴⁸ It is based on inelastic scattering of a monochromatic excitation source by molecules. In Raman scattering, the photon interacts with the molecule and polarizes the electrons around the nuclei to form an unstable virtual state. The photon is immediately released. During the scattering process, the nuclear motion is induced, resulting in transfer of energy from incident photon to molecule or vice versa.⁴⁹ In this

case the energy of the scattered photon is different from that of incident photon by one vibrational unit. It is a weak process as about 1 in 10^6 to 10^8 photons are scattered inelastically.⁵⁰ A plot of the intensity of scattered photons versus energy difference is a Raman spectrum. This spectrum can be used to identify the molecule, as each molecule provides a unique “molecular fingerprint”.⁵⁰

The main advantage of a Raman spectroscopy over a red, green, blue (RGB) flatbed scanner is the high-spatial resolution, as it is possible to attain a spatial resolution of $10\ \mu\text{m}$ (about the physical size of a human cell) with small uncertainty. When the film is scanned with a RGB flatbed scanner, the response differences are insignificant near the center of the scanner, but increase considerably towards the lateral edges.⁴⁰ Whereas, in Raman spectroscopy the response differences are insignificant throughout the ROI, as all the scanning points are equally excited by the laser. With Raman spectroscopy, we can observe the change in the molecular fingerprints of colorless monomer/polymers. Raman spectroscopy requires an approximately 2 minutes to scan an RCF area of $100 \times 100\ \mu\text{m}^2$ with a spatial resolution of $10\ \mu\text{m}$ whereas; a flatbed scanner takes a few minutes to read multiple films.

In resonance Raman spectroscopy, we select the wavelength of the exciting laser source to coincide with the electronic transition of a particular chromophoric group in a molecule. Raman intensities corresponding to this chromophore are selectively enhanced by a factor of 10^3 to 10^5 .⁵¹

The Vis-spectroscopy of RCF shows two distinct peaks at 635 and 585 nm.³¹ The absorption peak at 635 nm corresponds to the electronic transition

of the blue phase of the diacetylene polymer. In this experiment, we used 632.8 nm laser as an exciting source, which is close to the absorption peak of the blue phase, and it selectively enhances the vibrational bands associated with this phase. In other words, 632.8 nm laser enables us to examine the vibrational modes of blue phase due to resonance enhancement.

1.2.3. Confocal Raman Micro-Spectroscopy

Use of a confocal microscope considerably improves Raman micro-spectroscopy.⁵¹ In a conventional wide-field microscope, large light scattering blurs the image. By placing a pinhole aperture (10 to 100 micrometer in diameter) between the microscope objective and the image plane significantly rejects the residual scattered rays originated from out-of-focus on the sample (see Figure 4).⁵² The smallest pinhole aperture gives the best rejection. Besides significant improvement in lateral spatial resolution, it is possible to measure Raman spectra at different sample depths.⁵¹

Mirza et al. (2016) presents the work based on conventional Raman spectroscopy.¹⁶ In that study, we used the unlaminated RCF and acquired the Raman signal at the top of the film. The RCFs used in this study had a polyester matte layer on the top of the active layer (see Figure 2(b) and (c)) which sufficiently attenuate the Raman intensity.³⁹ A confocal Raman spectroscopy system was used to read these RCFs.

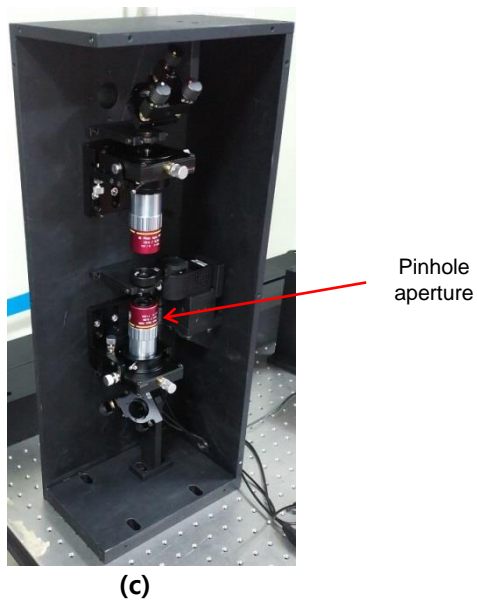
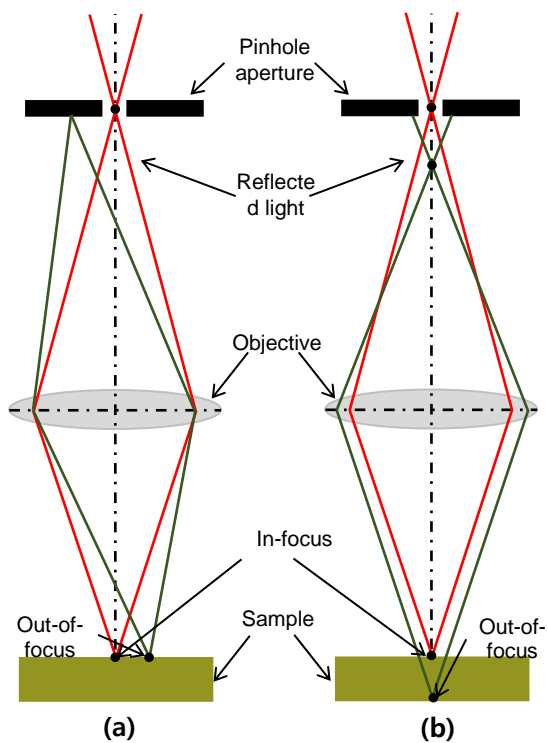


Figure 4. Pinhole aperture spatially filters the (a) horizontal and (b) vertical out-of-focus rays.⁵² (c) Pinhole aperture installed with Raman spectroscopy system at Seoul National University.⁵³

1.2.3.1. Spatial Resolution of Confocal Raman Microscopy

1.2.3.1.1. Lateral Spatial Resolution

The wavelength of the exciting laser and microscope objective defines the achievable spatial resolution of Raman micro-spectroscopy. Using Rayleigh criterion of contrast resolution, the lateral spatial resolution of Raman spectroscopy is defined as:⁵⁴

$$R = \frac{0.61\lambda}{NA} \quad (1)$$

where R is the lateral spatial resolution, λ is the wavelength of exciting laser and NA is the numerical aperture of the objective. The improved lateral spatial resolution by confocal Raman spectroscopy is defined as:⁵⁴

$$R = \frac{0.4\lambda}{NA} \quad (2)$$

The confocal mapping thus enhances the lateral resolution of the wide-field Raman mapping (see Figure 5). The confocal performance depends on the pinhole size.

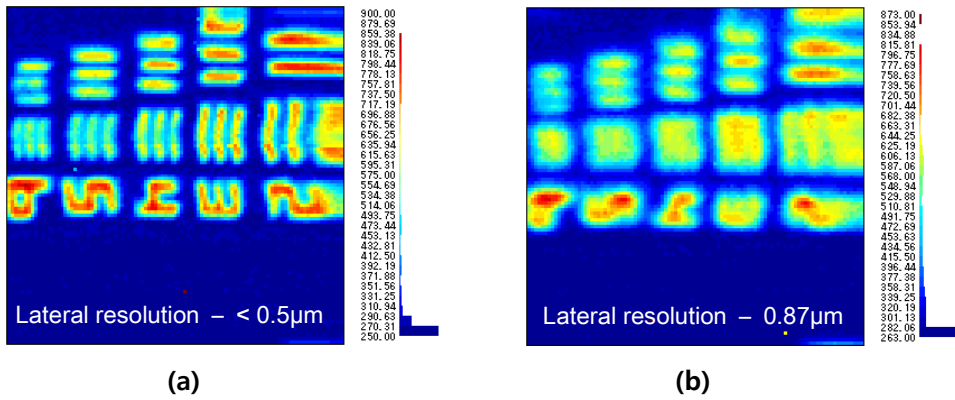


Figure 5. Confocal image of USAF target standard of group 9 elements 2, 3, 4, 5, and 6 (a) with pinhole size of $30\ \mu\text{m}$ and (b) without pinhole. The image size is $30 \times 30\ \mu\text{m}^2$ with spatial resolution of $300\ \text{nm}$. The objective lens used was Olympus $100\times$ magnification. Thickness of dashes for element 1, 2, 3, 4, 5, and 6 are 976.6 , 870 , 775.1 , 690 , 615.2 , and $548.1\ \text{nm}$, respectively.⁵³

1.2.3.1.2. Axial Spatial Resolution

The axial spatial resolution of confocal Raman microscopy is defined as:⁵⁵

$$\Delta z_{\text{confocal}} \sim \frac{4.4n\lambda}{2\pi NA^2} \quad (3)$$

Raman spectra of each film piece were measured by a Ramboss-star confocal Raman micro-spectroscopy system (Dongwoo Optron Co. Ltd, Korea) with the Raman shift range from 50 cm⁻¹ to 4200 cm⁻¹. This system was equipped with the Olympus BX53 microscope and BX3-URA illuminator with M Plan APO 100× objective of 0.70 numerical aperture (Mitutoyo Corp., Japan). A He-Ne laser (18 mW) operating at 632.8 nm with a power density of less than 3 mW/μm³ at the sampling point was used as a source of excitation. Measurements were taken using a 1,200 grooves/mm grating and 0.2-second laser exposure time, for ten accumulated spectra. Confocal microscope with 30 μm pinhole was used to reject out-of-focus signals, significantly improving the lateral resolution of the Raman spectroscopy system. For a He-Ne laser of 632.8 nm with 100× objective (Numerical Aperture 0.70), the lateral and axial resolutions of the confocal micro-Raman spectroscopy system are ~0.36 μm and ~0.90 μm, respectively.^{54,55} The Raman spectroscopy was calibrated with a silicon wafer at 520 cm⁻¹ before measurements.⁵⁶ Raman spectra of each film were recorded at a minimum of 24-hour post-irradiation. Data acquisition and processing were done using Andor SOLIS 4.16.30002.0 and Ramboss mapping 1.02, respectively.

1.2.3.2. Metallurgical vs Oil Immersion Objective

Over the years confocal Raman spectroscopy system was supplied with the metallurgical objectives.⁴¹ However, this resulted in poor depth resolution and significant degradation in the sensitivity because of severe spherical aberration. As shown in Figure 6 the rays refract and the focus shifts when the exciting laser source is focused a distance Δ below the surface of a transparent sample with refractive index n .⁴¹ The paraxial rays will focus at $n\Delta$ instead of Δ . Hence there will be a depth scale compression. The marginal rays are focused even deeper. The depth resolution (DR) is defined as the distance between paraxial and marginal foci and increase linearly with Δ . The DR relates to the NA of the objective lens, sample refractive index, and Δ :⁴¹

$$DR = \Delta \left\{ \left[\frac{NA^2(n^2 - 1)}{1 - NA^2} + n^2 \right]^{1/2} - n \right\} \quad (4)$$

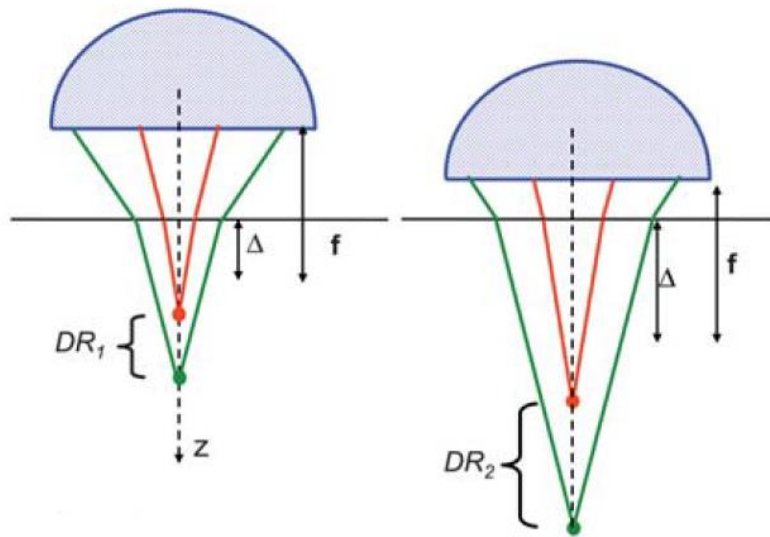


Figure 6. Illustration of spherical aberration of lens of focal length f when trying to focus the laser at a distance Δ below the ample surface. The surface refraction shifts the focus deeper into the sample at distance $n\Delta$. The depth resolution (DR) increase linearly with Δ .⁴¹

This spherical aberration causes extreme foreshortening of depth scale and degrades the depth resolution and signal to noise ratio as shown in Figure 7 (Lower). Using oil immersion objective with index matching fluid between the sample surface and the objective can minimize this foreshortening effect as shown in Figure 7 (Upper).⁴¹

This study presents the work with confocal Raman spectroscopy with the metallurgical objective. We did depth profiling of RCF to find the point of the maximum signal. We assumed that this maximum signal is coming from the top of the active layer. Radiological physics laboratory (RPLab) has recently purchased oil immersion objective and matching fluid. In future, all the experiments presented here will be repeated with the oil immersion objective.

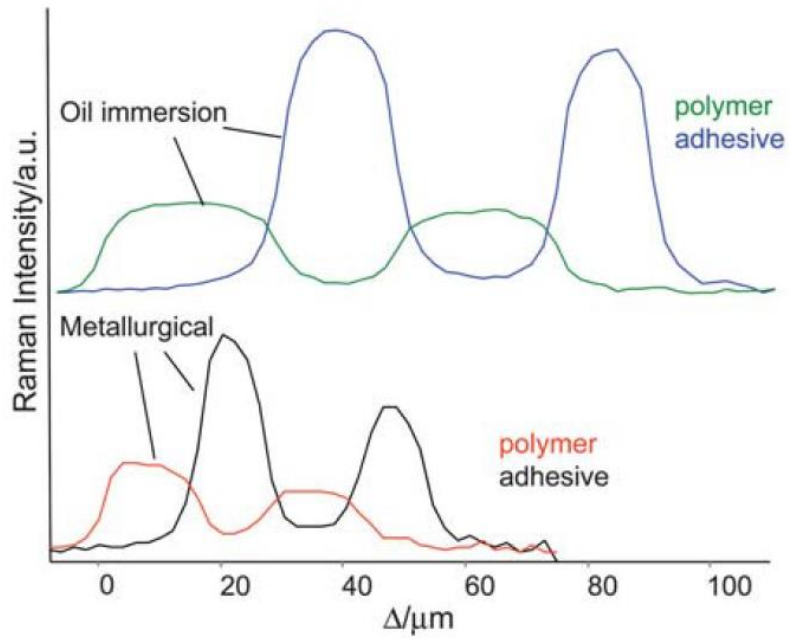


Figure 7. Depth profile through 4 layer polymer laminate using (Upper) 100 \times oil immersion objective and (Lower) 100 \times metallurgical objective.⁴¹

Keeping this phenomenon of spherical aberration in mind and assuming that n for our EBT-XD film is same as that of PET (i.e. ~ 1.6), we selected $\Delta = 60.85 \mu\text{m}$ when measured from the top of the polyester layer, such that we get the maximum Raman signal.^{41,57}

1.2.4. Data Acquisition and Analysis

The RCFs were placed on a motorized XYZ mapping stage to acquire Raman spectrums at different locations (smallest step size of the stage is $0.05 \mu\text{m}$).⁵³ Charged coupled device detectors used in Raman spectroscopy are susceptible to cosmic rays causing spurious spikes in measured spectra.⁵⁸ If these spikes coincide to the carbon triple band peak, we get Raman intensities higher than the expected one. Similarly, any dirt particle or micro-dent present in the active layer may result in Raman intensities lower than the expected one. We used Chauvenet's criterion to eliminate spurious data.⁵⁹

1.2.4.1. Raman Mapping

Raman mapping technique developed earlier was used to map a region of interest (ROI) of $10 \times 10 \mu\text{m}^2$ on each film with a spatial resolution of $10 \mu\text{m}$ (scanning time was about 100 seconds). Through this, Raman spectrums of 121 pixel points per ROI were obtained. The $\text{C}\equiv\text{C}$ peak of each film was preprocessed, which included band selection, smoothing and baseline removal.⁵¹ The sample generated dose-dependent fluorescence was removed by creating a smooth curve as a baseline and then subtracting it from the original Raman spectrum.^{37,60} We selected an identical range of carbon triple bond bands for all Raman spectra of exposed and unexposed RCF to consistently remove the baseline. The subtracted peak was then fitted with

Lorentzian peak function. Finally, the band heights for all dose levels were obtained to draw calibration curves. Microsoft Excel and Origin Pro 9 were used for this analysis.

1.2.4.2. Spatial Resolution

The spatial resolution of an imaging system describes how small an object can be seen.⁶¹ The response of the imaging system to a line input source is called line spread function (LSF). The LSF(x) is used to determine the modulation transfer function (MTF) in the experimental setting. The x is the positional variation along the x-axis. The MTF describes the spatial resolution and is the accepted standard for the characterization of spatial resolution. The frequency at which the MTF crosses the 10% level provides the spatial resolution of an imaging system. In some situations, the edge spread function (ESF) is more useful. The ESF(x) is the response of an imaging system to an edge gradient. The derivative of ESF(x) gives the LSF(x):⁶¹

$$LSF(x) = \frac{d}{dx}(ESF(x)) \quad (5)$$

The ESF(x) and LSF(x) is shown in Figure 8. Practically LSF(x) is used to determine the $MTF(f)$ (Figure 9). The LSF(x) is first normalized to have unity area:⁶¹

$$\int_{-\infty}^{\infty} LSF(x)dx = 1 \quad (6)$$

Then modulus of Fourier transform of $LSF(x)$ gives the $MTF(f)$

$$MTF(f) = \left| \int_{-\infty}^{\infty} LSF(x)e^{-2\pi ifx} dx \right| \quad (7)$$

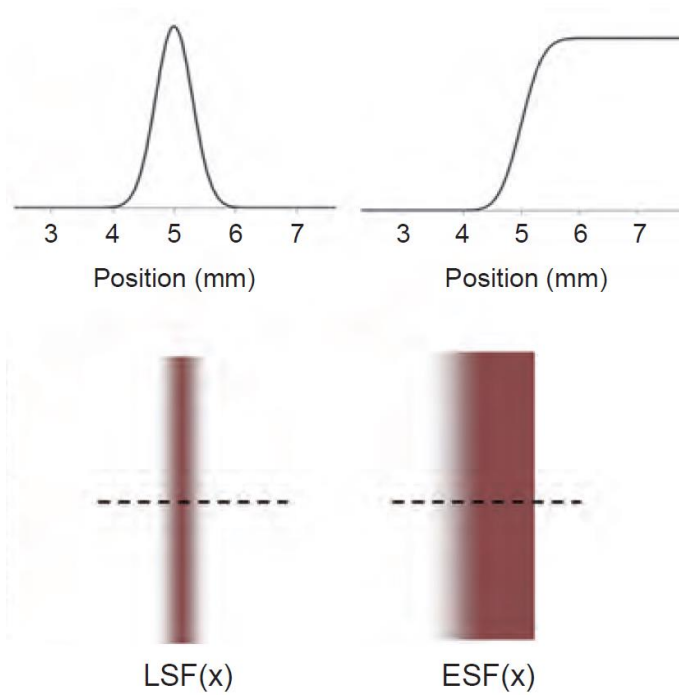


Figure 8. Line spread function (LSF) and edge spread function. A mathematical relationship exists between ESF and LSF. Fourier transform of LSF gives the spatial resolution of an imaging system.⁶¹

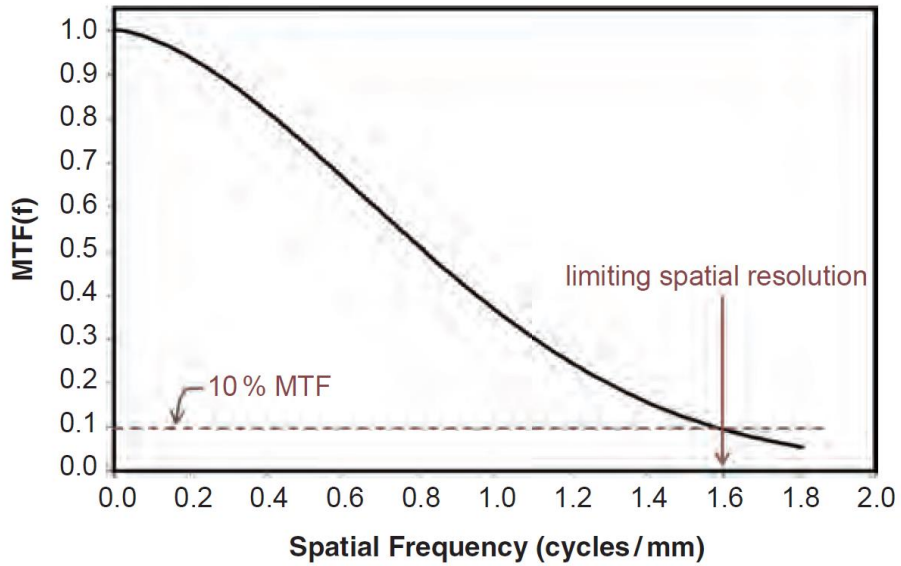


Figure 9. The limiting spatial resolution is the spatial frequency at which the amplitude of the modulation transfer function (MTF) decreases to some agreed-upon level. Here the limiting spatial resolution is shown at 10% modulation, and the limiting spatial resolution is 1.6 cycles/mm.⁶¹

A $1 \times 1 \text{ cm}^2$ GNF with thicknesses 50 and 100 nm were fabricated such that left half of each film was PET only and right half was PET coated with GNF. The GNF was then attached with the active layer of $3 \times 3 \text{ cm}^2$ unlaminate EBT-XD film. The tightly contacted GNF with RCF was then irradiated using 200 kVp X-rays, such that beam first enters in GNF. The LEE produced in GNF would cause dose enhancement in active layer as shown in Figure 10. The horizontal profiles of the films were taken using Raman spectroscopy. The data was acquired on an area of $2000 \times 10 \text{ }\mu\text{m}^2$ with spatial resolution of 10 μm . The horizontal profile was then fitted with the Sigmoidal Boltzmann function to get ESF(x). Using Eq. (5), (6) and (7) MTFs were determined.

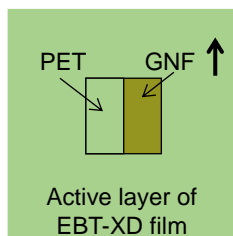


Figure 10. Schematic diagram of active layer of EBT-XD after irradiation. $1 \times 1 \text{ cm}^2$ GNF with thicknesses 50 and 100 nm were fabricated such that left half of each film was PET only and right half was PET coated with GNF. The GNF was then attached with the active layer of $3 \times 3 \text{ cm}^2$ unlaminate EBT-XD film.

1.2.4.3. Calibration Curves, Dose Ranges and Dosimetric Sensitivity

1.2.4.3.1. Calibration Curves using C≡C Band Heights

EBT3 and EBT-XD films were exposed to radiation doses between 0.3 and 30 Gy using 6 MV X-rays to obtain the calibration curves. The C≡C band heights corresponding to 121 points (ROIs of $100 \times 100 \mu\text{m}^2$) with a spatial resolution of $10 \mu\text{m}$ on each film were averaged and plotted as a function of dose. A statistical analysis using a lower-tailed independent two-sample t-test was done on all consecutive dose levels to find the clinically useful dose ranges of both dosimeter types. For dosimetric sensitivity, the fitted curves corresponding to calibration data of both types of RCFs were normalized from 0 to 1 and then compared.

1.2.4.3.2. Calibration Curves using Peak Ratio

Raman spectroscopy can be used to determine absorbed dose with a high spatial resolution as C≡C and C=C band heights in RCF increases with increasing dose due to polymerization. The band heights of the single peak were used for data manipulation. With the spatial resolution of $25 \mu\text{m}$, the dose variation for each dose level was less than 5%.¹⁶ However, a high variation is expected at increased spatial resolution due to the granular structure, compositional variations, stage movement, micro dents, scratches, or dust particles.³⁵ These variations at the microscopic level can be reduced if we take the ratio of two peaks from the Raman spectrum. Kamath et al.⁴⁸ used the ratio of polymer peak height to monomer peak height while using Fourier transform Raman spectroscopy. Figure 11 shows the Fourier transform spectra of diacetylene monomer, partial polymer, and 100% polymer. Table 1

presents the corresponding Raman shift values. The relative intensities of carbon triple bond monomer peak at 2220 cm^{-1} decreases and that of the polymer peak at 2123 cm^{-1} increase with increasing radiation dose (see Figure 12 (a)). A plot of the relative intensity ratio of polymer peak height to monomer peak height is presented in Figure 12 (b).

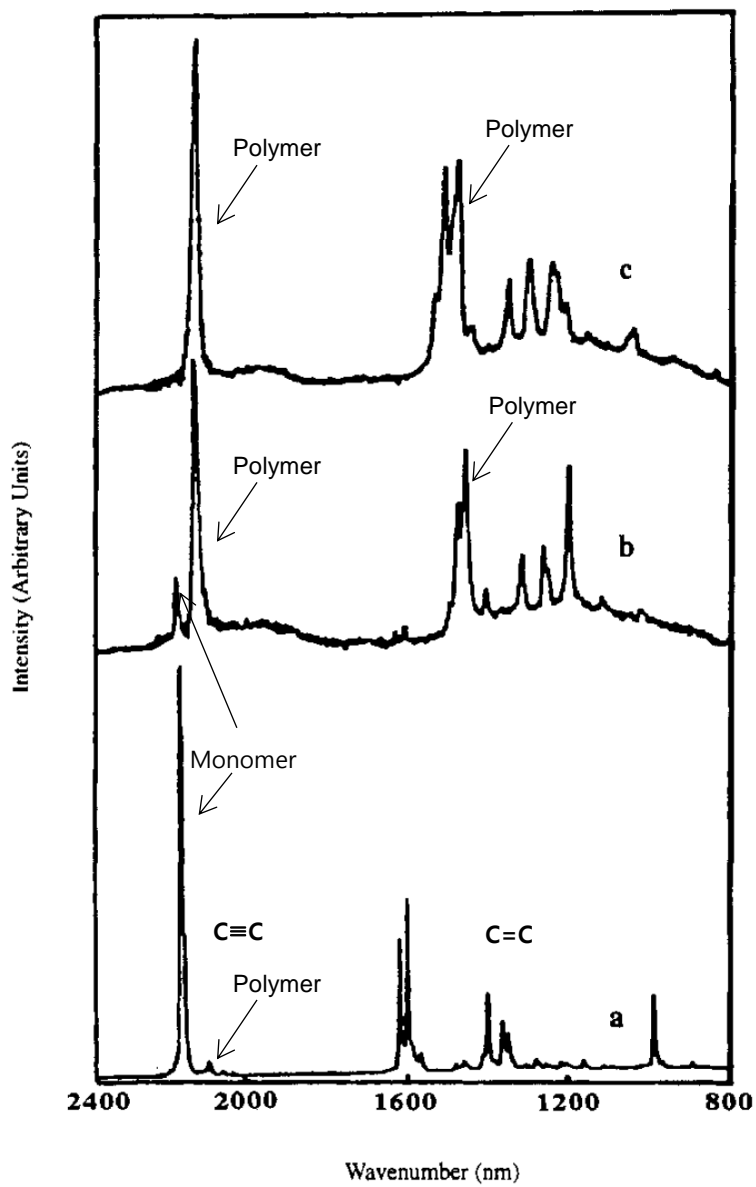


Figure 11. Fourier transform Raman spectra of (a) monomer, (b) partial polymer and (c) monomer free polymer (excitation wavelength is 1064 nm).⁴⁸

Table 1. Principal Raman vibrational bands of monomer, partial polymer and monomer free polymer^{a, 48}

Monomer	Partial polymer	Monomer free polymer
2220 (s) (C≡C)	2218 (w), 2123 (s)	2107 (s)
1617,1596 (m)	1620,1599 (vw)	
1415,1382,1368 (w) (C=C)	1493 (w), 1473 (s)	1493 (w), 1472 (s)
	1455 (s), 1408 (w)	1444 (8)
	1329,1279 (m)	
	1221 (8)	1195 (w)
1030 (w)	1148 (w)	1038 (w)

^a s = strong, m = medium, w = weak, vw = very weak.

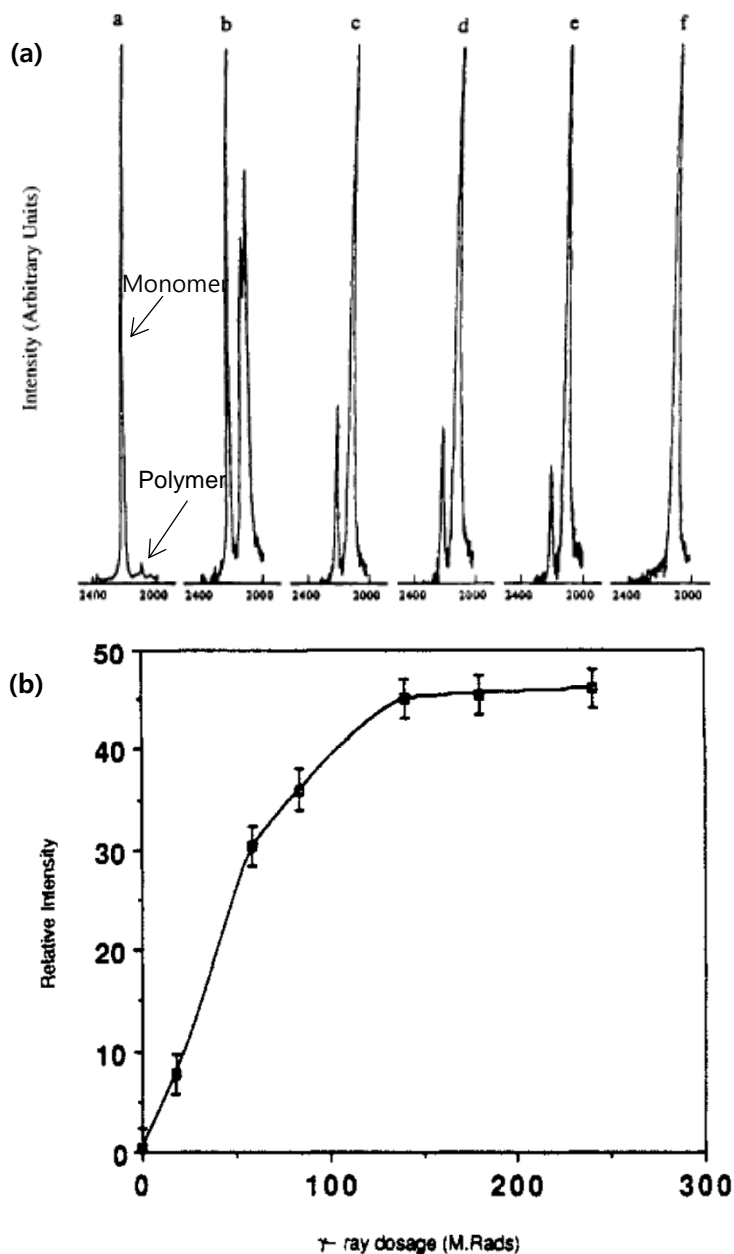


Figure 12. (a) Changes in the relative intensities of 2220 cm^{-1} ($\nu_{\text{C}=\text{C}}$ of monomer) and 2123 cm^{-1} ($\nu_{\text{C}\equiv\text{C}}$ of polymer) bands as a function of γ -ray dosage in the partial polymer: (i) 0 Mrad; (ii) 18 Mrad (iii) 59 Mrad; (iv) 84 Mrad; (v) 140 Mrad; (vi) 100% polymer. (b) Plot of relative intensities of the 2123 cm^{-1} band with respect to the 2220 cm^{-1} band as a function of γ -ray dosage in the partial polymer (relative intensity = ratio of polymer peak height to monomer peak height multiplied by 10).⁴⁸

However, the conventional Raman spectroscopy cannot distinguish the monomer peak from the polymer peak. With our Raman spectroscopy system at Seoul National University, we took the ratio of C≡C stretching band peak height to C-C-C deformation band peak height for EBT-XD films. Figure 13 shows the location of both peaks in a Raman spectrum of RCF.

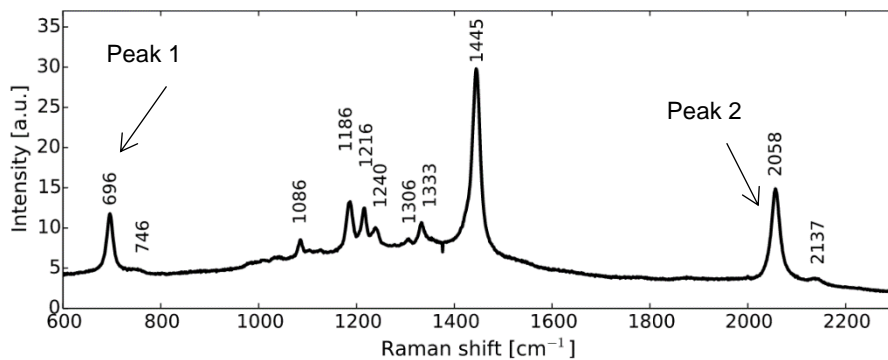


Figure 13. Raman spectrum of radiochromic film.³² The peak 1 at 696 cm⁻¹ corresponds to a C-C-C deformation peak whereas the peak 2 at 2058 cm⁻¹ belongs to the C≡C peak.

1.2.4.4. Dose Uniformity

The band heights of 121 pixel points in a ROI of $100 \times 100 \mu\text{m}^2$ with a spatial resolution of $10 \mu\text{m}$ were averaged for each dose level (0 to 30 Gy from 6 MV X-rays). The associated standard deviations (SD) and relative standard deviations (RSD) were considered as the measure of the dose uniformity.

1.2.4.5. Effect of Orientation of Radiochromic Films

The needle-like particles on the active layer of the RCF are dichroic in nature. Therefore, the laser beam polarizes differently with film orientation.¹⁶ The landscape and portrait orientations of film pieces were defined according to those of a full-length RCF sheet. We marked each cut piece of film with an arrow on the top right corner to indicate the landscape orientation. During Raman spectroscopy data acquisition, each film piece has landscape orientation if it is placed on the motorized stage such that the arrow is on the top right corner and it has portrait orientation if it is at the bottom left side of the film pointing to the right. For 6 MV X-rays, we acquired data with both landscape and portrait orientation to estimate the effect of film orientation on Raman data ($\text{C}\equiv\text{C}$ band heights). For quantification, orientation response ratio OR was calculated as:

$$OR = \frac{BH_{6\text{MV}}(D, P)}{BH_{6\text{MV}}(D, L)} \quad (8)$$

where $BH_{6\text{MV}}(D, P)$ and $BH_{6\text{MV}}(D, L)$ are the $\text{C}\equiv\text{C}$ band heights for portrait and landscape orientations of film on motorized XYZ sample stage at a given dose D , respectively. The subscript of BH shows that the films were

exposed with 6 MV X-rays. The uncertainty in OR is expressed as error propagation resulted from the division of terms in Eq. (8).

1.2.4.6. Energy and Dose Rate Dependence

The $2 \times 2 \text{ cm}^2$ RCF pieces were irradiated to doses of 0.3, 0.5, 1, 2, 4 and 6 with X-rays energies of 50, 100, 200 and 300 kVp, and 6 MV to check the energy dependence of EBT3 and EBT-XD RCFs. To quantify the energy dependency of both types of RCF dosimeters, we defined energy response ratio ER as:

$$ER = \frac{BH_x(D)}{BH_{6\text{ MV}}(D)} \quad (9)$$

where $BH_x(D)$ and $BH_{6\text{ MV}}(D)$ are the C \equiv C band heights of X-rays energy under investigation and that of 6 MV at a given dose D , respectively.

Both RCF types were tested for the dose rate dependence using 200 kVp X-rays with dose rates of $32.26 \text{ mGy}\cdot\text{s}^{-1}$ and $16.13 \text{ mGy}\cdot\text{s}^{-1}$, for doses from 0.3 to 6 Gy. For quantification, we defined dose-rate response ratio as:

$$DR = \frac{BH_{(200\text{ kVp}, 16.13\text{ mGy}\cdot\text{s}^{-1})}(D)}{BH_{(200\text{ kVp}, 32.26\text{ mGy}\cdot\text{s}^{-1})}(D)}, \quad (10)$$

where $BH_{(200\text{ kVp}, 16.13\text{ mGy}\cdot\text{s}^{-1})}(D)$ and $BH_{(200\text{ kVp}, 32.26\text{ mGy}\cdot\text{s}^{-1})}(D)$ are the C \equiv C band heights for 200 kVp X-rays with dose-rates of $16.13 \text{ mGy}\cdot\text{s}^{-1}$ and $32.26 \text{ mGy}\cdot\text{s}^{-1}$ at a given dose D , respectively.

1.2.4.7. Post-Irradiation Stability

When the RCF is exposed to ionization radiations, the color changes immediately, however, it requires at least 24 hours to become stable.⁴⁶ The $2 \times 2 \text{ cm}^2$ pieces of RCFs were irradiated to doses of 0.5 and 2 Gy using 200 kVp X-rays, Raman data was acquired after 0.5, 1, 2, 6, 24 and 168 h to check the post-irradiation phenomenon. For quantification of post-irradiation stability, we defined Post-irradiation dose response PR as:

$$PR = \frac{BH_{(200 \text{ kVp}, x \text{ hours})}(D)}{BH_{(200 \text{ kVp}, 168 \text{ hours})}(D)}, \quad (11)$$

where $BH_{200 \text{ kVp}, x \text{ hours}}(D)$ and $BH_{(200 \text{ kVp}, 168 \text{ hours})}(D)$ are the $\text{C}\equiv\text{C}$ band heights for 200 kVp X-rays measured after x hours ($x = 0.5, 1, 2, 6, 24$ hours) and 168 hours, respectively.

1.3. Results

1.3.1. Assignment of Raman Peaks of Active Layer of Radiochromic Film

Figure 14 shows the Raman spectrum of the active layer of an RCF irradiated at 1 Gy. On the basis of available multiple studies on the vibrational mode of diacetylene polymer, Callens et al. allocated bands in the Raman spectrum of RCF.³² This includes δ_{CCC} deformation and $\nu_{\text{C-C}}$, $\nu_{\text{C=C}}$, $\nu_{\text{C}\equiv\text{C}}$ stretching modes of polymer backbone at 694, 1087, 1446, and 2060 cm^{-1} respectively. $\nu_{\text{C-C}}$ corresponding to the alkyl side chain also contributes in the peak at 1087 cm^{-1} . The peak series from 1190 to 1340 cm^{-1} are assigned to CH_2 wagging and CH_2 twists modes of all trans-alkyl chain. The polymeric bands in the Raman spectrum of the 0 Gy film suggest the presence of polymer prior to irradiation. This can originate from exposure to UV or background radiation or elevated temperatures.³² Diacetylene polymers exhibit bluish green, blue and red phases. Raman peaks δ_{CCC} deformation and $\nu_{\text{C-C}}$, $\nu_{\text{C=C}}$, $\nu_{\text{C}\equiv\text{C}}$ stretching modes of polymer backbone at 694, 1087, 1446, and 2060 cm^{-1} , respectively are assigned to the blue phase. For the red phase, we can assign peaks at 748 and 2142 to C-C-C and C-triple bond, respectively.³² The red phase peaks corresponding to C-C and C=C are hidden in the Raman spectrum presented in Figure 4.

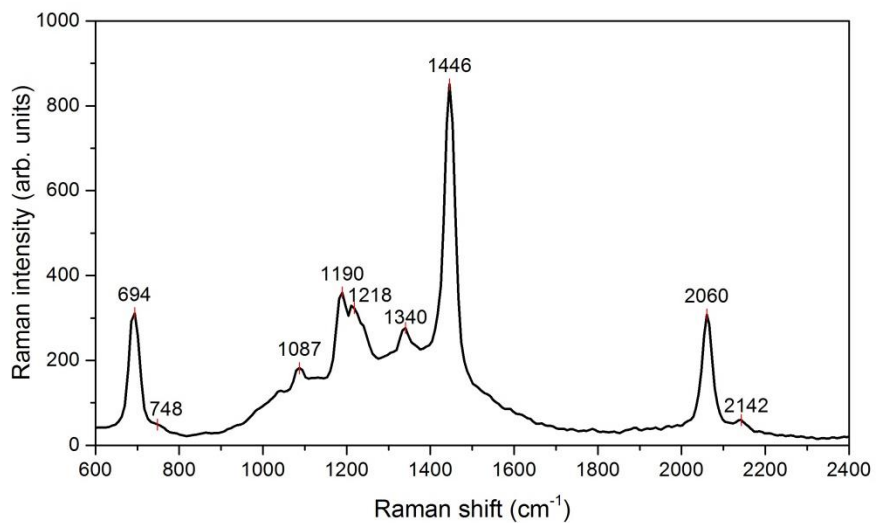


Figure 14. The Raman spectrum of active layer of a radiochromic film (EBT-XD) irradiated with a dose of 1 Gy. The centers of prominent peaks are noted above the peaks.

1.3.2. Spatial Resolution

Figure 15 (a) and (b) show the edge spread functions (ESFs) for the GNFs of thicknesses 50 and 100 nm, respectively (see Figure 10). Black solid line represents the original horizontal profile when scanning with step of 10 μm is done from no gold area to gold coated area ($10 \times 2000 \mu\text{m}$). Figure 15(c) and (d) present their corresponding modulation transfer functions (MTFs). The spatial resolution at 10% modulation was 54 and 50 μm respectively.

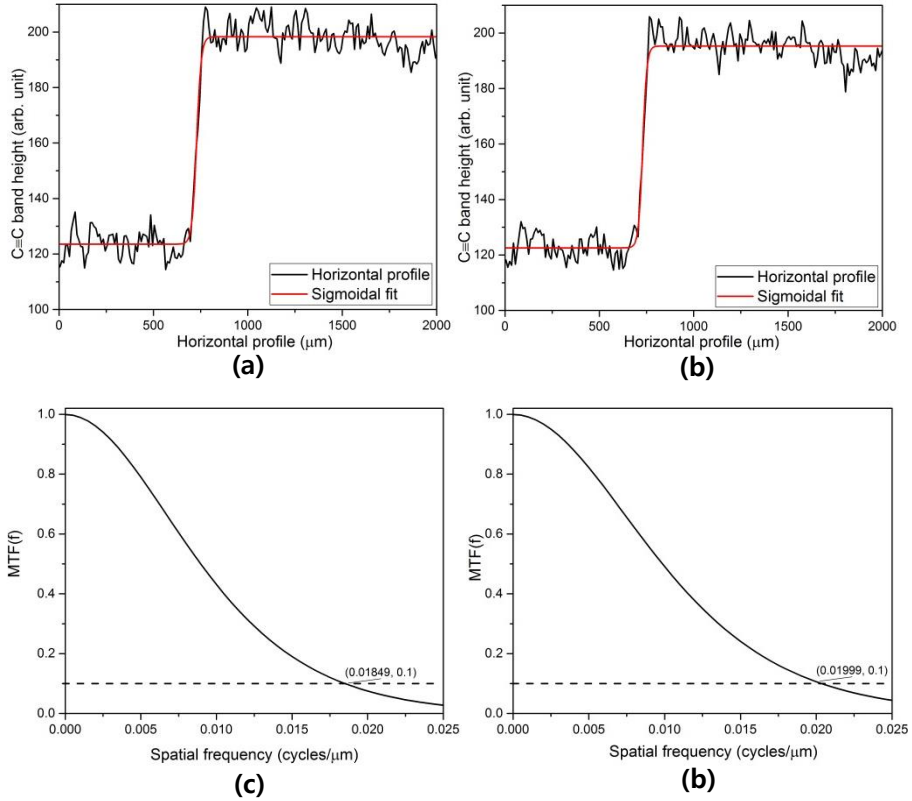


Figure 15. (a) and (b) shows the edge spread functions (ESFs) for the GNFs of thicknesses 50 and 100 nm, respectively. Black solid line represents the original horizontal profile when scanning with step of 10 μm is done from no gold area to gold coated area ($10 \times 2000 \mu\text{m}$). (c) and (d) presents the modulation transfer functions (MTFs) for (a) and (b) respectively. The spatial resolution at 10% modulation is (a) 0.01849 cycles/ μm and (b) 0.01999 cycles/ μm , which is equivalent to (a) $\sim 54 \mu\text{m}$ and (b) $\sim 50 \mu\text{m}$.

1.3.3. Dose Calibration and Dosimetric Sensitivity

The mean C≡C band height values extracted from Raman mapping data of EBT3 and EBT-XD films at different dose values are presented in Figure 16(a) and Table 2. The error bars indicate one standard deviation of the mean of 121 pixels at a region of interest of $100 \times 100 \mu\text{m}^2$ on each film with a spatial resolution of $10 \mu\text{m}$. Each solid black square and red circle represent one data point of EBT3 and EBT-XD Gafchromic film, respectively corresponding to single dose level. The data points for both EBT3 and EBT-XD were fitted with two component exponential functions and are displayed by solid black and red lines respectively in Figure 16(a). The fitted curves of Figure 16(a) were normalized from 0 to 1 range to compare the sensitivity of both film types and are shown in Figure 16(b). From Figure 16(b), it can be inferred, that for all the dose points, type EBT-3 film is more sensitive than EBT-XD film, however, the Raman response of type EBT-3 film saturates earlier.

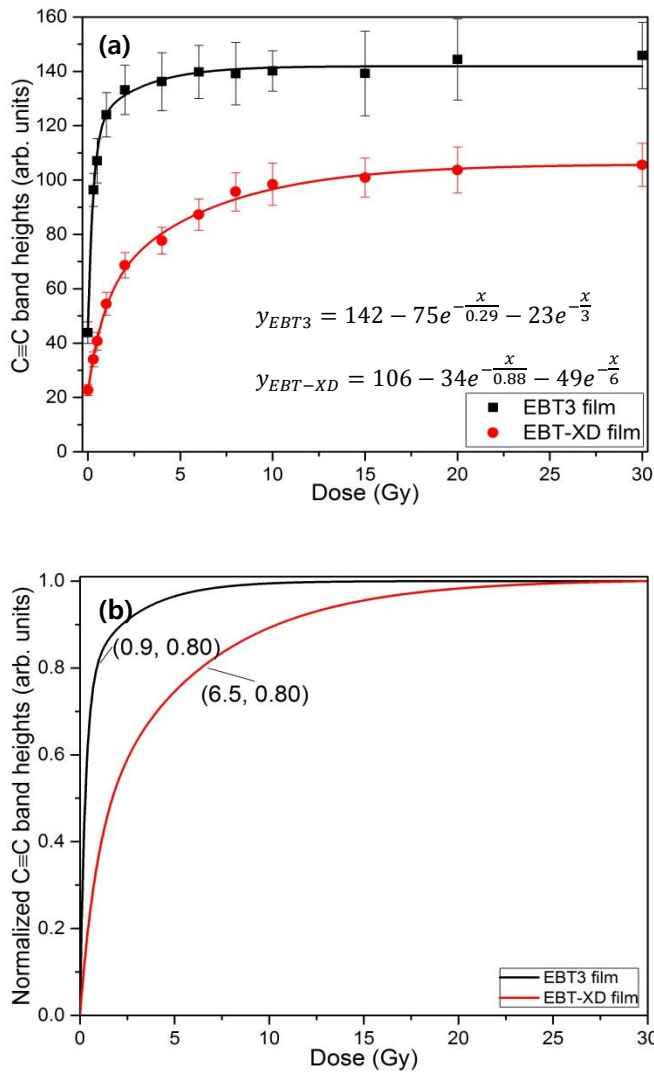


Figure 16. (a) Dose calibration curves with band heights of carbon triple bond (0-30 Gy, 6 MV X-rays). Each black square and red circle represent data point of EBT3 and EBT-XD Gafchromic film, respectively. Error bars indicate one standard deviation of the mean of 121 pixels at region of interest of $100 \times 100 \mu\text{m}^2$ on each film with spatial resolution of $10 \mu\text{m}$. EBT3 and EBT-XD curves are fitted by an exponential functions of two components with R-squared values of 0.9987 and 0.9985 respectively. The solid lines represent fitted curves. (b) For comparison, the fitted curves of both types of radiochromic films as shown in Figure 16(a) are normalized from 0 to 1. It can be inferred that EBT3 is more sensitive than EBT-XD but saturates earlier.

Table 2. Mean, standard deviation (SD), and relative standard deviation (RSD) from measured Raman mapping data of 121 pixels of C≡C peaks around 2060 cm⁻¹ for region of interest of 100 × 100 μm² with spatial resolution of 10 μm at radiation doses ranging from 0 to 30 Gy for both types of radiochromic films (for 6 MV X-rays). These values were calculated after applying preprocessing steps to all peaks.

C≡C Band heights at ~2060cm ⁻¹ (arb. units)						
Dose (Gy)	EBT3 Film			EBT-XD Film		
	Mean	SD	RSD (%)	Mean	SD	RSD (%)
0	44	4	9.2	23	2	9.0
0.3	96	6	6.3	34	3	8.1
0.5	107	8	7.6	41	3	8.0
1	124	8	6.6	54	4	7.9
2	133	9	6.8	69	5	6.8
4	136	11	7.8	78	5	6.4
6	140	10	7.0	87	6	6.6
8	139	12	8.3	96	7	7.4
10	140	7	5.3	98	8	7.9
15	139	16	11.2	101	7	7.1
20	144	15	10.4	104	8	8.1
30	146	12	8.4	106	8	7.5

Figure 17(a) and (b) show the calibration curves when C≡C stretching band peak height and ratio of C≡C peak height to C-C-C peak height are plotted as a function of dose, respectively. Table 3 presents the mean, SD and RSD for C-C-C and C≡C band heights, and their peak ratios. From Table 3, we can infer that by peak ratio method the RSD can be reduced to 3%. However, peak ratio method gives calibration curve less sensitive to C≡C band height method. This study is based on single peak method. Peak ratio method is left for future work.

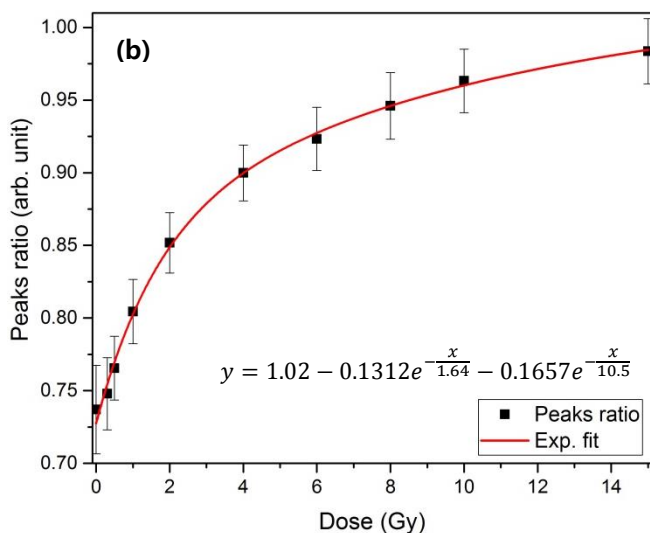
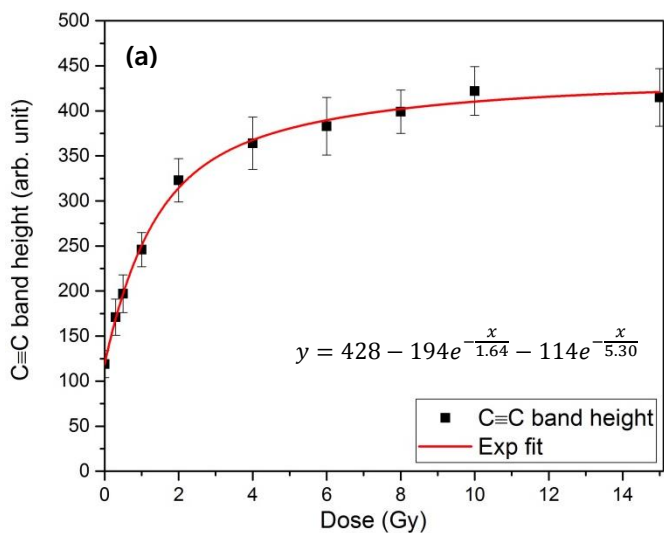


Figure 17. Dose response with respect to (a) C≡C band height and (b) ratio of C≡C stretching band peak height to C-C-C deformation band peak height. Dose response with C≡C band height is more sensitive than that of Peak ratio method, however, the standard deviation is ~3% in case of Peak ratio dose response.

Table 3. Mean, standard deviation (SD), and relative standard deviation (RSD) for C-C deformation peak (Peak 1), C≡C stretching peak (Peak 2) and their ratio (Peak 2 / Peak 1). Peak ratio method has least variation but less sensitive than C≡C peak method. The data is acquired with 150 grooves/mm grating.

Dose (Gy)	Peak 1 at 696 cm ⁻¹			Peak 2 at 2058 cm ⁻¹			Peak 2 / Peak 1		
	Mean	SD	RSD (%)	Mean	SD	RSD (%)	Mean	SD	RSD (%)
0	119	15	12.7	88	11	12.0	0.7370	0.0304	4.1
0.3	171	20	12.0	128	15	11.9	0.7479	0.0248	3.3
0.5	197	21	10.5	151	17	11.0	0.7655	0.0220	2.9
1	246	19	7.8	198	17	8.8	0.8045	0.0221	2.7
2	323	24	7.5	276	22	8.1	0.8518	0.0208	2.4
4	364	29	8.0	327	27	8.2	0.8999	0.0192	2.1
6	383	32	8.3	354	30	8.6	0.9233	0.0218	2.4
8	399	24	6.0	377	22	5.9	0.9460	0.0229	2.4
10	422	27	6.4	406	27	6.7	0.9632	0.0218	2.3
15	415	32	7.6	409	32	7.8	0.9836	0.0225	2.3

1.3.4. Dose Range

In Figure 16(a), the error bars overlap at high dose end of both types of film dosimeters. We first assessed the normality using the Kolmogorov-Smirnov test and then performed a statistical analysis using a lower-tailed independent two-sample t-test on all consecutive dose levels lying in the error bars overlapping region.⁶² The results of the statistical analysis at a significance level of 0.05 are presented in Table 4 and Table 5 for EBT3 and EBT-XD films, respectively. The results show that the dose-response saturates at ~6 Gy for EBT3 film, however, EBT-XD has higher dose range.

Table 4. Student t -test for EBT3 film. The lowered tailed independent two sample t -test on consecutive dose maps in a region where error bars start overlapping in Figure 16(a). Significance level = 0.05, null hypothesis: mean I – mean II \geq 0, and alternative hypothesis: mean I – mean < 0.

Dose groups			Equal variance assumed			Unequal variance assumed		
I (Gy)	II (Gy)	MD ^a	t -statistics	df ^b	p -value	t -statistics	df	p -value
4	6	-4	-2.709	236	0.004	-2.709	234	0.004
6	8	1	0.462	236	0.678	0.462	230	0.678
8	10	-1	-0.749	237	0.227	-0.747	201	0.228
10	15	1	0.534	239	0.703	0.536	172	0.704
15	20	-5	-2.608	239	0.005	-2.608	239	0.005
20	30	-1	-0.812	237	0.209	-0.813	229	0.209

^aMD is mean difference.

^bdf is degrees of freedom.

Table 5. Student *t*-test for EBT-XD film. The lowered tailed independent two sample *t*-test on consecutive dose maps in a region where error bars start overlapping in Figure 16(a). Significance level = 0.05, null hypothesis: mean I – mean II \geq 0, and alternative hypothesis: mean I – mean < 0.

Dose groups			Equal variance assumed			Unequal variance assumed		
I (Gy)	II (Gy)	MD ^a	<i>t</i> -statistics	df ^b	<i>p</i> -value	<i>t</i> -statistics	df	<i>p</i> -value
4	6	-10	-13.955	237	0.000	-13.947	231	0.000
6	8	-8	-9.995	235	0.000	-9.986	225	0.000
8	10	-3	-2.876	236	0.002	-2.878	235	0.002
10	15	-2	-2.527	239	0.006	-2.526	237	0.006
15	20	-3	-2.773	240	0.003	-2.773	234	0.003
20	30	-2	-1.809	238	0.036	-1.810	238	0.036

^aMD is mean difference.

^bdf is degrees of freedom.

1.3.5. Dose Uniformity

SDs and RSDs from measured Raman mapping data of 121 pixels of $C\equiv C$ peaks around 2060 cm^{-1} for a region of interest of $100 \times 100\ \mu\text{m}^2$ at radiation doses ranging from 0 to 30 Gy for both types of RCFs are presented in Table 2 to assess the dose uniformity at a spatial resolution of $10\ \mu\text{m}$. Ignoring the data points at saturation region, the dose non-uniformity at a microscopic level is less than 10 % for both types of film dosimeters. From Table 3, we can infer that by peak ratio method significantly reduces the dose uniformity (i.e. $\sim 3\%$).

1.3.6. Effect of Radiochromic Film Orientation

Figure 18 and Table 6 present the effect of film orientation on $C\equiv C$ band heights for a given dose. The film dosimeters were measured with landscape and portrait orientation. For both RCF types, a curve with landscape orientation was found more sensitive than that with portrait orientation. The variation due to orientation was higher at low doses. For EBT3 and EBT-XD films, at 0.5 Gy the portrait orientation underestimated the landscape orientation by 30% and 36% respectively, and at 6 Gy these underestimations were reduced to 7% and 19% respectively.

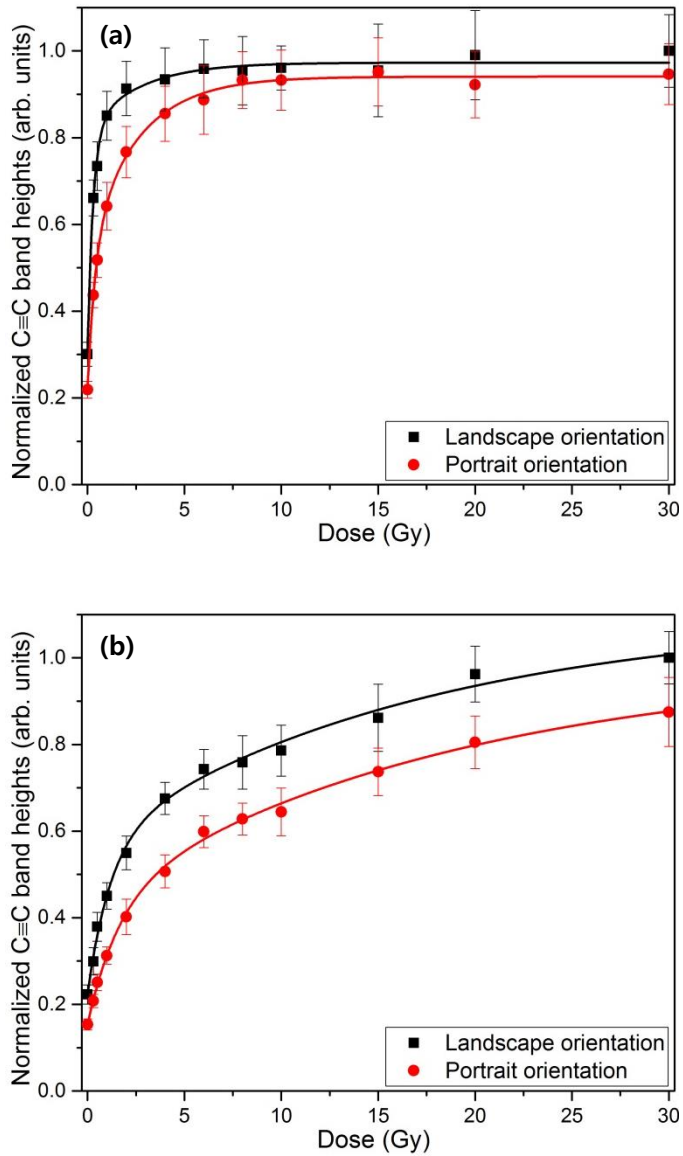


Figure 18. Normalized dose response of (a) EBT3 and (b) EBT-XD film with different orientation. In case of both radiochromic film types, the films measured with landscape orientation have higher sensitivity than that with portrait orientation. The curves are normalized to the average values of C≡C band height of landscape orientation at 30 Gy.

Table 6. Orientation response ratio for quantification of effect of film orientation when readout by Raman spectroscopy.

Dose (Gy)	Orientation response ratio	
	EBT3	EBT-XD
0	0.73 ± 0.09	0.69 ± 0.09
0.3	0.66 ± 0.06	0.69 ± 0.09
0.5	0.70 ± 0.08	0.66 ± 0.08
1	0.76 ± 0.08	0.69 ± 0.06
2	0.84 ± 0.09	0.73 ± 0.09
4	0.92 ± 0.10	0.75 ± 0.07
6	0.93 ± 0.11	0.81 ± 0.07
8	0.98 ± 0.11	0.83 ± 0.08
10	0.97 ± 0.09	0.82 ± 0.09
15	1.00 ± 0.14	0.86 ± 0.10
20	0.93 ± 0.12	0.84 ± 0.08
30	0.95 ± 0.11	0.87 ± 0.10

1.3.7. Energy Dependence

Figure 19 and Table 7 and 8 present the energy response, for kVp X-rays for doses in the 0.3 to 6 Gy range. Figure 19(a) and (b) show the variation of C≡C band heights with dose for EBT3 and EBT-XD, respectively, for X-rays energies of 50, 100, 200 and 300 kVp, and 6 MV. The energy response ratios for EBT3 and EBT-XD film demonstrate energy dependence of less than or equal to 9% (see Table 7 and 8) with micrometer spatial resolution.

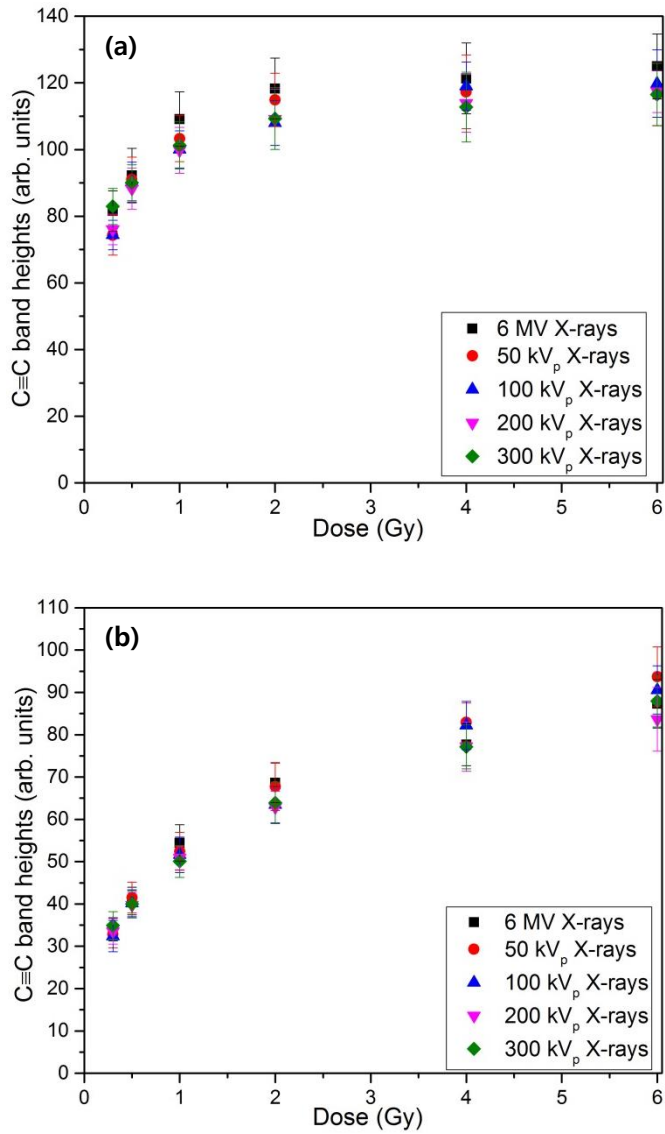


Figure 19. Variation of Carbon triple bond band heights with dose to observe the energy dependence for (a) EBT3 film and (b) EBT-XD film. Error bars indicate one standard deviation of the mean of 121 pixels at region of interest of $100 \times 100 \mu\text{m}^2$ on each film with spatial resolution of $10 \mu\text{m}$.

Table 7. Energy response ratios for type EBT-3 film to compute the energy dependence of various kVp X-rays relative to 6 MV X-rays.

kVp	Energy response ratios for EBT-3 film at variable doses					
	0.3 Gy	0.5 Gy	1 Gy	2 Gy	4 Gy	6 Gy
50	0.91 ± 0.10	0.99 ± 0.11	0.95 ± 0.10	0.97 ± 0.10	0.97 ± 0.12	0.93 ± 0.10
100	0.91 ± 0.09	0.98 ± 0.11	0.92 ± 0.09	0.91 ± 0.09	0.98 ± 0.10	0.96 ± 0.11
200	0.93 ± 0.09	0.96 ± 0.11	0.91 ± 0.09	0.92 ± 0.10	0.94 ± 0.11	0.94 ± 0.09
300	1.02 ± 0.10	0.98 ± 0.10	0.93 ± 0.10	0.92 ± 0.11	0.93 ± 0.12	0.93 ± 0.10

Table 8. Energy response ratios for EBT-XD film to compute the energy dependence of various kVp X-rays relative to 6 MV X-rays.

Energy response ratios for EBT-XD film at variable doses						
kVp	0.3 Gy	0.5 Gy	1 Gy	2 Gy	4 Gy	6 Gy
50	0.97 ± 0.12	1.02 ± 0.12	0.96 ± 0.11	0.99 ± 0.11	1.07 ± 0.09	1.07 ± 0.11
100	0.95 ± 0.13	0.99 ± 0.11	0.95 ± 0.11	0.92 ± 0.09	1.06 ± 0.10	1.04 ± 0.09
200	0.99 ± 0.12	0.98 ± 0.11	0.93 ± 0.09	0.92 ± 0.08	0.99 ± 0.10	0.96 ± 0.11
300	1.03 ± 0.12	0.98 ± 0.11	0.92 ± 0.10	0.93 ± 0.10	0.99 ± 0.09	1.01 ± 0.10

1.3.8. Dose Rate Dependence

Figure 20 and Table 9 present the effect of dose rate on EBT3 and EBT-XD films when irradiated by 200 kVp X-rays. For both film types and for all doses the variations are less than 5%.

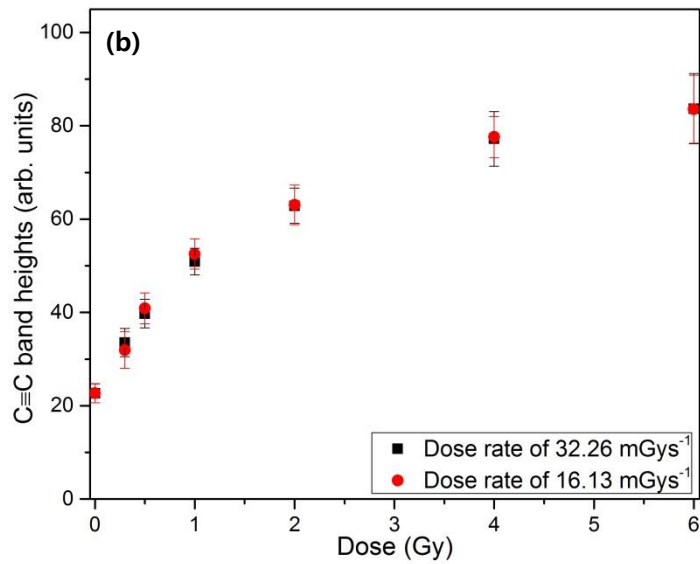
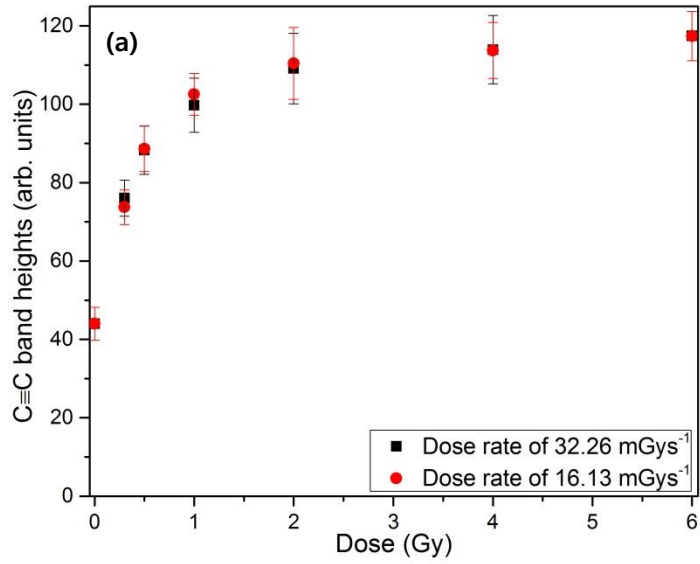


Figure 20. Variation of Carbon triple bond band heights with dose to observe the dose rate dependence for (a) EBT3 film, and (b) EBT-XD film, when irradiated at 200 kVp X-rays. Error bars indicate one standard deviation of the mean of 121 pixels at region of interest of $100 \times 100 \mu\text{m}^2$ on each film with spatial resolution of $10 \mu\text{m}$.

Table 9. Dose rate response ratios of radiochromic films to observe the dose rate dependence of two different types of radiochromic films.

Film Type	DR ^a (16.13 mGy·s ⁻¹) / DR (32.26 mGy·s ⁻¹) of radiochromic films w.r.t. doses					
	0.3 Gy	0.5 Gy	1 Gy	2 Gy	4 Gy	6 Gy
EBT3	0.97 ± 0.08	1.00 ± 0.10	1.03 ± 0.09	1.01 ± 0.12	1.00 ± 0.1	1 ± 0.08
EBT-XD	0.95 ± 0.15	1.03 ± 0.12	1.04 ± 0.09	1.00 ± 0.09	1.01 ± 0.1	1 ± 0.13

^aDR is dose rate.

1.3.9. Post-Irradiation Stability

Figure 21 shows the change in carbon triple bond band heights with time when EBT3 and EBT-XD films were exposed to 0.3 and 0.5 Gy by 200 kVp X-rays. Post-irradiation response ratios of both film types were calculated to compare the time variation of doses with respect to stable dose response taken after one week and presented in Table 10. The variations in carbon triple bond band heights between 1 and 24 hours after irradiation were between 1% and 8% for all doses under study. Between 24 and 168 hours after irradiation, the variations carbon triple band heights were less than 2% except EBT-XD film exposed to 0.5 Gy, which was reduced by 11%.

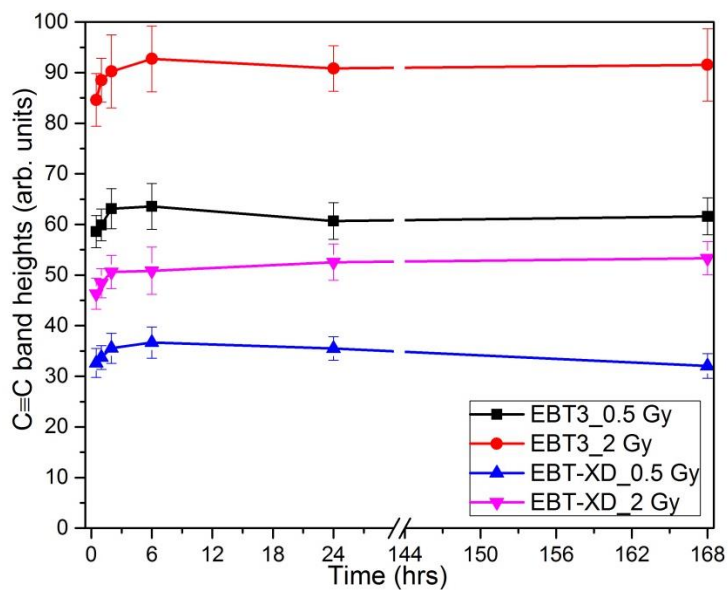


Figure 21. Change of the carbon triple bond band heights as a function of time since irradiation for EBT3 and EBT-XD films exposed to 0.5 Gy and 2 Gy at 200 kVp. Error bars indicate one standard deviation of the mean of 121 pixels at region of interest of $100 \times 100 \mu\text{m}^2$ on each film with spatial resolution of $10 \mu\text{m}$.

Table 10. Post-irradiation response ratio of radiochromic films w.r.t. stable dose readings taken after one week.

Time (hours)	EBT3		EBT-XD	
	0.5 Gy	2 Gy	0.5 Gy	2 Gy
0.5	0.95 ± 0.08	0.92 ± 0.09	1.02 ± 0.12	0.87 ± 0.08
1	0.97 ± 0.08	0.97 ± 0.09	1.05 ± 0.11	0.91 ± 0.08
2	1.02 ± 0.09	0.99 ± 0.11	1.11 ± 0.13	0.95 ± 0.08
6	1.03 ± 0.1	1.01 ± 0.11	1.14 ± 0.13	0.95 ± 0.11
24	0.98 ± 0.08	0.99 ± 0.09	1.11 ± 0.11	0.99 ± 0.09

1.4. Discussion

The results of our work suggest that Raman spectroscopy can be used to determine absorbed dose with a high-spatial resolution by exploiting the idea that $C\equiv C$ and/or $C=C$ in EBT3 films increase with increasing dose due to polymerization of diacetylene monomer. Christopher G. Soares (2007) proposed that the color producing elements of the film emulsion (chromophores) are approximately $0.75\ \mu\text{m}$ in diameter, which should be considered as the absolute limit of film resolution.³⁴ Also, depending on the laser wavelength, microscope objectives and confocal pinholes used during Raman spectroscopy, an intrinsic spatial resolution of $< 1\ \mu\text{m}$ are achievable.³⁷ It is, therefore, possible to develop a novel microdosimetry system using RCFs and a Raman spectroscopy in conjunction with a microscope.

Theoretically, it is possible to achieve a spatial resolution of fewer than $10\ \mu\text{m}$ while reading RCF by Raman spectroscopy.^{34,37} Figure 14 shows that 10% MTF corresponds a spatial resolution of $50\ \mu\text{m}$ when tightly contacted $100\ \text{nm}$ GNF with RCF was irradiated using $200\ \text{kVp}$ X-rays. We hypothesize that this comparatively poor resolution can be attributed to the angular distribution of low energy electrons, non-uniformity of the gold layer near the edges of PET substrate, and wide-field irradiation condition. For better spatial resolution we may require highly collimated X-rays with a shielding system that can make ESF with sharp edges of having penumbra less than or equal to $10\ \mu\text{m}$. A micro-densitometer or microscope with an appropriate objective and light source can be used to achieve very high spatial resolution.³⁵

However, reading out with Raman spectroscopy is advantageous in a sense that dose variation is less than 3% when data is acquired with micrometer spatial resolution. Moreover, with Raman spectroscopy, we can analyze polymerization in colorless polymers. The document scanner or densitometer cannot analyze colorless films. Also, at low doses, the calibration curves obtained by Raman microscopy are more sensitive than document scanner or densitometer.

From Figure 16 and Table 4 and Table 5, we can infer that while using the confocal Raman mapping technique the clinically useful range for EBT3 and EBT-XD is up to ~6 and ~20 Gy, respectively. The EBT3 film is more sensitive but saturates earlier than EBT-XD film. For micrometer resolution dosimetry by confocal Raman spectroscopy, we recommend using EBT3 film for doses up to ~2 Gy and EBT-XD film for high doses (greater than 2 Gy). Lewis et al.⁴⁰ also reported that EBT-XD is less sensitive than EBT3 when measured with RGB flatbed scanner and showed that EBT3 exposed to 10 Gy and EBT-XD exposed to 40 Gy have the same response value. Likewise, for Raman spectroscopy, an EBT3 film exposed to 0.3 Gy and an EBT-XD exposed to 9 Gy have the same carbon triple bond band height values. For a dose range of 0 to 30 Gy, the EBT3 and EBT-XD films achieved 80% of carbon triple bond band heights at 0.9 and 6.5 Gy, respectively as shown in Figure 16 (b). This variation is due to the size difference of chromophores in their corresponding active layers.⁴⁰ The length to width ratios of EBT3 and EBT-XD films are approximately 1:10 and 1:2 respectively (see Figure 3). During the film coating procedure, the long axis of chromophores tends to align parallel to fluid flow followed by Brownian motion just before the

coating is dried. The large particles in an EBT3 film are comparatively less affected by Brownian.⁴⁰ The higher number of chromophores in EBT3 film maintained preferential alignments when compared to those of EBT-XD film causing different sensitivity levels.

Table 2 presents the means, SDs, and RSDs calculated from 121 data points of C≡C band heights in a region of interest of $100 \times 100 \mu\text{m}^2$ with a spatial resolution of $10 \mu\text{m}$ at radiation doses ranging from 0 to 30 Gy for both types of film. For clinically useful dose ranges, both types have dose non-uniformity of less than 10%. At a macroscopic level, the dose non-uniformity is less than 1% when measured with the flatbed scanner and after applying the correction methods suggested by Saur et al.⁴³ However, a high variation is expected at a microscopic level due to the granular structure, compositional variations, micro dents, scratches, or dust particles.³⁵ In Raman mapping, variation by stage movement may be an additional reason for the dose non-uniformity of the films. Table 3 presents the means, SDs, and RSDs using peak ratio method. This method significantly reduces the dose non-uniformity (~3%) at micrometer level. However this method is less sensitive than C≡C band height method.

RCFs showed different dose responses with the orientation due to preferential alignment of chromophores in the active layer.⁶³ Figure 18 and Table 6 showed that the C≡C band heights response for both RCF types in landscape orientation is more sensitive than those in portrait orientation for all dose levels.

The purpose to introduce new models of RCF by the manufacturer is to make them more water equivalent by varying the chemical compositions. The water equivalency may deviate at low energies because of the photoelectric effect of the high Z -elements in the active layer.⁶⁴ In addition to this absorbed dose energy dependence, RCFs also have intrinsic energy dependence.^{65,66} Recently, Hammer et al.⁶⁴ considered microdosimetric interactions to determine intrinsic energy response. Figure 19 shows that for both RCF types, the low energy X-rays exhibit weak energy dependence with respect to 6 MV X-rays. The energy response ratio presented in Table 7 and Table 8 show that the low energy X-rays can result in underestimation of up to 9% in RCFs under study. At micrometer resolution, this variation can be due to the intrinsic non-uniformity of the film. Villarreal-Barajas *et al*⁶⁷ noted that response ratio with respect to a ^{60}Co beam at 1 Gy decreases monotonically; however, we did not see such trend. In this study, we found that there is no significant energy interdependency for low energy X-rays. Massillon-JL et al.¹⁵ and Brown et al.⁶⁸ reported the energy dependence of maximum 11% and 3%, respectively. Recently, Hammer et al.⁶⁴ compared the different versions of the EBT3 film and reported that any compositional change in the active layer could result in different energy response. In this study other than the compositional variation amid different versions, the dose non-uniformity at a μm level resolution and different measuring technique may also contribute to the difference in results from previous studies.

Figure 20 and Table 13 present the effect of dose rate on EBT3 and EBT-XD films when irradiated by 200 kVp X-rays. For both film types and for all

doses the variations are less than 5%. Similar to previous studies about RCFs, both EBT3 and EBT-XD films are dose rate independent.^{46,69}

Post-irradiation responses of RCFs are presented in Figure 21 and Table 10. All other films under study showed a stable response after 24 hours post-irradiation except EBT-XD film exposed to 0.5 Gy showing consistency with previous work.^{46,70} On the basis of post-irradiation stability results, we recommend using EBT3 for low doses and EBT-XD film above 0.5 Gy when measured by Raman spectroscopy.

Sizes of most human cells range from 2 μm to 120 μm .⁷¹ Raman mapping technique when applied on RCF, is an upgraded option when we want to measure doses at a μm level. A spatial resolution of 10 μm is achievable within 10% of uncertainties by confocal Raman spectroscopy. Compared to Flatbed optical scanner Raman microscopy may be considered as a time-consuming and tedious job, however with the advent of new technology, a very fast mapping (less than 100 msec. at each point) is within reach.⁴¹

1.5. Conclusions

This study has demonstrated that both the EBT3 and EBT-XD films are suitable micrometer resolution dosimetry by confocal Raman spectroscopy. Cellular level spatial resolution is theoretically possible as both the radiochromic film and Raman spectroscopy has the spatial resolution of less than 1 micrometer. A 100 nm gold nanofilm tightly contacted with the active layer of radiochromic film exhibited the spatial resolution of 50 μm when irradiated with 200 kVp X-rays. The angular distribution of low energy electrons, non-uniformity of the gold layer near the edges of PET substrate, and wide-field irradiation condition may degrade the spatial resolution of the imaging system. A spatial resolution of 10 μm is achievable within 10% of dose non-uniformity. The EBT-XD film is less sensitive than the EBT3 film. As the $\text{C}\equiv\text{C}$ band heights for EBT3 film saturates earlier, we recommend EBT3 film for doses less than 2 Gy and EBT-XD film for high doses. The dose-response for the RCFs measured in landscape orientation is more sensitive than those measured in portrait orientation. The EBT3 and EBT-XD films show weak energy dependency compared to previous versions. Both types of RCFs are dose rate independent and show a stable response after 24 hours post-irradiation. Peak ratio method significantly reduces the effect of dose non-uniformity. In future, this work will be extended to achieve a micrometer resolution with greater dose uniformity.

Chapter II

2. Application of Raman Spectroscopy to Measuring the Radioenhancement of Gold Nanofilm

2.1. Introduction

Previous studies have shown that an existence of ^{79}Au - / ^{64}Gd - NPs near the tumor, increases the cell-killing when exposed to low-energy photons.^{23-29,72} The mechanism of this efficient cell-killing is still unclear; however possible reasons may include macro- and micro-scale dose enhancement explained above, generation of reactive oxygen species, cell cycle effects, DNA damage, and cytoplasmic events.²⁹ The main source for the radioenhancement of NPs is abundant LEEs as their relative biological effectiveness is greater than one.^{36,73}

The dose enhancement factor (DEF) of metal NPs is defined as the ratio of a dose in the presence of metal NPs to that without metal NPs.²⁶ Earlier studies using biological in vitro and animal models examined the macroscopic dose enhancement by metal NPs.⁷⁴ Rakowski et al. recently combined experimental results of EBT2 Gafchromic™ film and Monte Carlo (MC) modeling and found a DEF of 18.31 within the first 0.25 μm water depth from 23.1 nm-thick gold nanofilm (GNF).³⁶ More recent studies considered microscopic dose distributions and used microscopic DEFs to predict cell

survival for various ionizing radiation beams.⁷⁵⁻⁷⁷ Experimental quantification of microscopic DEF in the immediate vicinity of metal NPs is limited due to nanoscale ranges of LEEs. Therefore, MC simulations are most widely used to predict microscopic DEFs.⁷⁴

The purpose of this study is to experimentally measure the macroscopic DEF of GNFs for low- and high-energy X-rays. The experimental results were then compared with analytical calculations. Radiation dose enhancements from the NPs were first analytically calculated by Roeske et al.⁷⁸ In this study, the same approach was used to calculate the radiation dose enhancement caused by GNF on the RCF. The advantage of using GNFs over gold nanoparticles (GNPs) was to measure an area-averaged dose rather than a point dose. GNFs with the thickness equivalent to the size of GNPs were expected to show similar interactions with ionizing radiation.

2.2. Methods and Materials

2.2.1. Preparation of Gold Nanofilm

A 188 μm -thick polyethylene terephthalate (PET) film was cut into $1 \times 1 \text{ cm}^2$ pieces as coating substrates for GNFs. The PET substrates were rinsed with distilled water after washing in an ultrasonic cleaner with ethanol as a cleaning solvent. GNFs were prepared using a thermal evaporation technique. The gold was heated and vaporized under vacuum condition in a thermal evaporator (Centus OL100). The evaporated gold particles moved up and deposited on the PET substrate to form a thin layer of gold. GNFs with nominal thicknesses of 20, 30, 40, 50, and 100 nm were prepared by adjusting the deposition time.

The actual thicknesses of deposited gold layer on PET substrates were measured with Alpha-Step profiler (Alpha-Step IQ surface profiler, KLA Tencor).⁷⁹ Alpha-Step is a stylus-based surface profiler, which can scan the surface status of a sample. Slits were made at three randomly selected areas of each nanofilm sample. The depth from the surface of GNF to the surface of substrate at a slit was measured as the thickness of GNF. The depth of each slit was measured 10 times and averaged using a step analysis mode with multi-scans. The scan speed was 20 $\mu\text{m}/\text{second}$ with a sampling rate of 100 Hz. The estimated gold-thicknesses were used in the following MC simulations.

2.2.2. Preparation of RCF Samples

EBT-XD Gafchromic™ films (Ashland Specialty Ingredients, Bridge Water, NJ, USA) are a suitable radiochromic dosimeter due to their high spatial resolution, near-tissue equivalence, low energy dependence and dose-rate independence, and can be readout using an optical flatbed scanner, a microdensitometer, and a Raman micro-spectrometer.^{40,68} In this study, the EBT-XD films were used to measure the macroscopic DEF caused by photon interactions with GNFs.

The film has an active layer of 25 μm , which is sandwiched between two matte polyester substrates of 125 μm .^{38,42} When it is exposed to radiation, it reacts to form a blue colored polymer in its active layer.³² A matte polyester substrate from one side of the EBT-XD film was carefully removed to avoid the energy loss of incident radiation in this protective layer. This unlaminated EBT-XD film was cut into $3 \times 3 \text{ cm}^2$ pieces. A $1 \times 1 \text{ cm}^2$ piece of GNF was placed in direct contact with the active layer of the unlaminated EBT-XD film and attached tightly by using an adhesive tape. The orientation of GNF was adjusted so that the coated side of GNF contacted the active layer of the unlaminated EBT-XD film. A piece of PET film (without gold) was placed together next to the GNF for comparison (also see Figure 22). For calibration, pieces of the unlaminated EBT-XD film attached to PET film were also prepared.

2.2.3. Sample Irradiation and Calibration

X-ray beams of 50 and 220 kVp, (X-RAD 320 Biological Irradiator, Precision X-Ray, Inc., N. Branford, CT) and flattening filter free (FFF) 6 MV

(Truebeam[®], Varian Medical System, Palo Alto, CA) were used to deliver 0.3, 0.5, 1.0, and 1.5 Gy to the prepared samples of RCF attached to GNF and PET film. The active layer of the RCF, placed in direct contact with the GNF can absorb the energy of LEEs emitted as a result of the X-ray interactions with GNF.³⁶ For calibration, the prepared pieces of RCF attached to PET film were irradiated with doses of 0.3, 0.5, 1.0, 1.5, 2.0, 4.0, 6.0, and 8.0 Gy. All the samples of RCF were irradiated in air at 50 cm source-to-surface distance (SSD) for 50 and 220 kVp beams and at 5 cm depth in solid water at 100 cm source-to-axis distance (SAD) for 6 MV FFF with a field size of $10 \times 10 \text{ cm}^2$ (Figure 22).

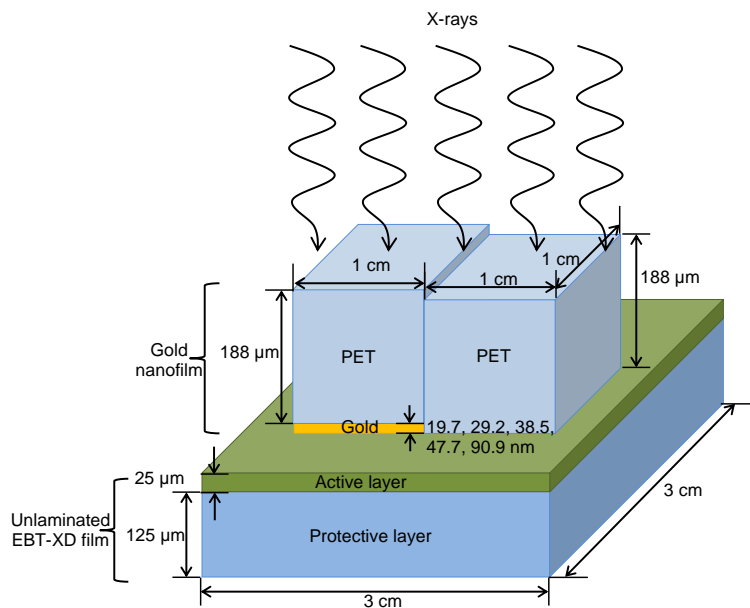


Figure 22. Schematic of GNF and unlaminate EBT-XD film irradiated by X-rays (not scaled). On the active layer of the unlaminate EBT-XD film, GNF and PET without gold were irradiated by X-ray beams. PET without gold was used as a control to calculate DEF. Beneath this geometry 5 cm solid water was placed for backscatter. For 6 MV FFF beam, a 5 cm build-up phantom was additionally placed on the top of this geometry.

2.2.4. Radiochromic Film Reading

The GNF and PET film were removed from the unlaminated EBT-XD film once exposed to the X-ray beams. These unlaminated RCFs were then readout by using an optical flatbed scanner and a confocal Raman spectrometer.

2.2.4.1. Optical Flatbed Scanner

The RCFs were scanned using a flatbed scanner (Expression 11000XL Epson, Tokyo, Japan). The scanner was operated in the transmission mode at 1200 dpi and 48 bits red-green-blue channels. The scanned images were saved in TIFF format. The central region of the scanner was used during film scan to evade the lateral response artifact.^{43,80} ImageJ v1.51n software (National Institutes of Health, Bethesda, MD, USA)^{44,45} was used to obtain the optical densities from the scanned images. The red channel was adopted due to its better sensitivity and stability over the other channels.

For each of unlaminated EBT-XD films, a mean value of scanner response was obtained from five separated regions of $2 \times 2 \text{ mm}^2$ area in the film. The mean scanner response was then converted to a dose by the manufacturer's recommendation as below:³⁸

$$R(D) = a + \frac{b}{D - c}, \quad (12)$$

where $R(D)$ was a scanner response from an irradiated film at a dose D , and a, b, c were the equation parameters for fitting. The scanner responses were then plotted against radiation doses to obtain the calibration curve.

2.2.4.2. Raman Spectroscopy

Raman spectra of each film piece were measured by Ramboss-star microscope Raman system (Dongwoo Optron Co. Ltd, Gyeonggi-Do, Korea) with the Raman shift range of 50 cm^{-1} to 4200 cm^{-1} . This system was equipped with the Olympus BX53 microscope and BX3-URA illuminator with M Plan APO 100 \times objective of 0.70 numerical aperture (Mitutoyo Corp., Japan). A He-Ne laser operating at 632.8 nm was used as a source of excitation. Measurements were taken using a 1200 grooves/mm grating with 0.2 sec laser exposure time and repeated ten times for accumulation. A confocal microscope with a 30 μm pinhole was used, which significantly improved the lateral resolution. For a He-Ne laser of 632.8 nm with 100 \times objective (Numerical Aperture 0.70), the lateral resolution of the confocal micro-Raman spectroscopy system was determined $\sim 0.36\text{ }\mu\text{m}$.⁵⁴ The Raman spectroscopy was calibrated with a silicon wafer at 520 cm^{-1} prior to measurements.⁵⁶ Raman spectra of each film were recorded at minimum of 24 hours post-irradiation. Data acquisition and processing were done using Andor SOLIS 4.16.30002.0 (Andor, United Kingdom) and Ramboss mapping 1.02 (DongWoo Optron, Gyeonggi-Do, Korea), respectively. Raman spectra at different points on RCF were acquired by placing the film on the Märzhäuser motorized XY mapping stage (Märzhäuser Wetzlar GmbH & Co. KG, Germany) with an electrically powered Z-axis focus (minimum step size of stage was $0.05\text{ }\mu\text{m}$).

The previously developed Raman mapping technique was used to map a region of interest (ROI) of $100 \times 100\text{ }\mu\text{m}^2$ on each film with a spatial resolution of $10\text{ }\mu\text{m}$ (scanning time was $\sim 100\text{ sec}$).¹⁶ A spatial resolution of 10

μm was chosen to observe the radioenhancement by GNF at a cellular level. Through this, Raman spectra of 121 pixel points per ROI were obtained. The $\text{C}\equiv\text{C}$ peaks of each pixel point were preprocessed, which included band selection, smoothing and baseline removal.⁵² Thereafter the subtracted peak was fitted with the Lorentzian peak function. The band heights (i.e., Raman intensity values at the peak of Lorentzian distribution) corresponding to 121 points on each film were averaged and the averaged values were plotted as a function of dose to draw the calibration curve.

2.2.5. Macroscopic Dose Enhancement Factor

In order to estimate the microscopic dose enhancement on the vicinity of GNP, nano or micrometer scale dosimetry is required. There is no such device available for this purpose, except for Monte Carlo simulation. The dosimetry proposed in this study using RCF was actually macroscopic dose estimation that measured an averaged dose on a relatively wide region of interest. A macroscopic dose enhancement factor is defined as a ratio of the dose deposited in RCF with GNF divided by the dose deposited in the RCF without GNF (i.e. PET only):

$$\text{Macroscopic DEF} = \frac{D_{\text{GNF}}}{D_{\text{PET}}}, \quad (13)$$

where D_{GNF} is the averaged value of estimated doses measured from regions of RCF exposed under GNF and D_{PET} is that exposed under PET film only.

2.2.6. Analytical Approach

2.2.6.1. Analytical Macroscopic Dose Enhancement Factor

From the knowledge of basic principles of radiation dosimetry, the collisional kerma for a photon beam of energy E that irradiates a medium of the atomic number Z is related to the energy fluence ψ by the mass energy absorption coefficient $(\mu_{\text{en}}/\rho)_{E,Z}$. Under the charged particle equilibrium (CPE) condition, the absorbed dose D is equal to the collisional kerma. Therefore, an absorbed dose to the medium is:⁴

$$D = \psi \cdot \left(\frac{\mu_{\text{en}}}{\rho} \right)_{E,Z} \quad (14)$$

In order to estimate the mass energy absorption coefficient of a uniform mixture, RCF (i.e., EBT-XD film), the additivity rule was applied below:⁴

$$\left(\frac{\mu_{\text{en}}}{\rho} \right)_{E,\text{EBTXD}} = f_{Z_1} \left(\frac{\mu_{\text{en}}}{\rho} \right)_{E,Z_1} + f_{Z_2} \left(\frac{\mu_{\text{en}}}{\rho} \right)_{E,Z_2} + \dots, \quad (15)$$

where f_{Z_i} represents the fractional weight compositions of individual elements in the active layer of RCF (see Table 11).

Table 11. Density and fractional weight composition of PET and EBT-XD films.⁴²

	Density (g/cm ³)	Fractional composition by weight								
		H	Li	C	N	O	S	Na	Cl	Al
PET	1.38	0.042		0.625		0.333				
Active layer	1.35	0.089	0.006	0.532	0.009	0.291	0.005	0.004	0.006	0.059
Protective layer	1.35	0.042		0.625		0.333				

Now consider a region of interest (ROI) on GNF attached to EBT-XD film, and the masses of GNF and EBT-XD film under this ROI. It was assumed that the effective mass energy absorption coefficient of GNF and EBT-XD film was given by

$$\begin{aligned} & \left(\frac{\mu_{\text{en}}}{\rho} \right)_{\text{E,eff}} \\ &= \frac{m_{\text{EBTXD}}}{m_{\text{EBTXD}} + m_{\text{Au}}} \left(\frac{\mu_{\text{en}}}{\rho} \right)_{\text{E,EBTXD}} + \frac{m_{\text{Au}}}{m_{\text{EBTXD}} + m_{\text{Au}}} \left(\frac{\mu_{\text{en}}}{\rho} \right)_{\text{E,Au}}, \end{aligned} \quad (16)$$

where m_{EBTXD} and m_{Au} represent the mass of the active layer of EBT-XD film and of GNF under the ROI, respectively.

A dose enhancement factor (DEF) is defined as the ratio of the dose deposited in EBT-XD film with GNF divided by the dose deposited in EBT-XD film without GNF. Using Eqs. (13) and (14), the DEF for a monoenergetic photon beam is:

$$DEF = \frac{\psi \left(\frac{\mu_{\text{en}}}{\rho} \right)_{\text{E,eff}}}{\psi \left(\frac{\mu_{\text{en}}}{\rho} \right)_{\text{E,EBTXD}}} \quad (17)$$

Inserting Eq. (16) into Eq. (17), then a macroscopic quantity of DEF is given by:

$$\frac{\frac{m_{\text{EBTXD}}}{m_{\text{EBTXD}} + m_{\text{Au}}} \left(\frac{\mu_{\text{en}}}{\rho} \right)_{\text{E,EBTXD}} + \frac{m_{\text{Au}}}{m_{\text{EBTXD}} + m_{\text{Au}}} \left(\frac{\mu_{\text{en}}}{\rho} \right)_{\text{E,Au}}}{\left(\frac{\mu_{\text{en}}}{\rho} \right)_{\text{E,EBTXD}}} \quad (18)$$

Simplifying Eq. (18):

$$\frac{1}{m_{\text{EBTXD}} + m_{\text{Au}}} \left(m_{\text{EBTXD}} + m_{\text{Au}} \left(\frac{\left(\frac{\mu_{\text{en}}}{\rho} \right)_{\text{E,Au}}}{\left(\frac{\mu_{\text{en}}}{\rho} \right)_{\text{E,EBTXD}}} \right) \right) \quad (19)$$

For simplicity, the effective energies E_{eff} of 50 and 220 kVp and 6 MV FFF polyenergetic photon beams were evaluated by equating to the energy of a monoenergetic X-ray beam that is attenuated as the same rate as the polyenergetic beam. The E_{eff} of 50 and 220 kVp and 6 MV FFF polyenergetic photon beams was determined to be 25.6, 48.3 and 1970 keV. The mass energy absorption values corresponding to E_{eff} were applied in Eq. (15) to calculate the DEF for 50 and 220 kVp, and 6 MV FFF photon beams. Eqs. (19) and (20) are fully valid if gold having a mass m_{Au} is uniformly mixed with the active layer of EBT-XD film as shown in Figure 23(a).

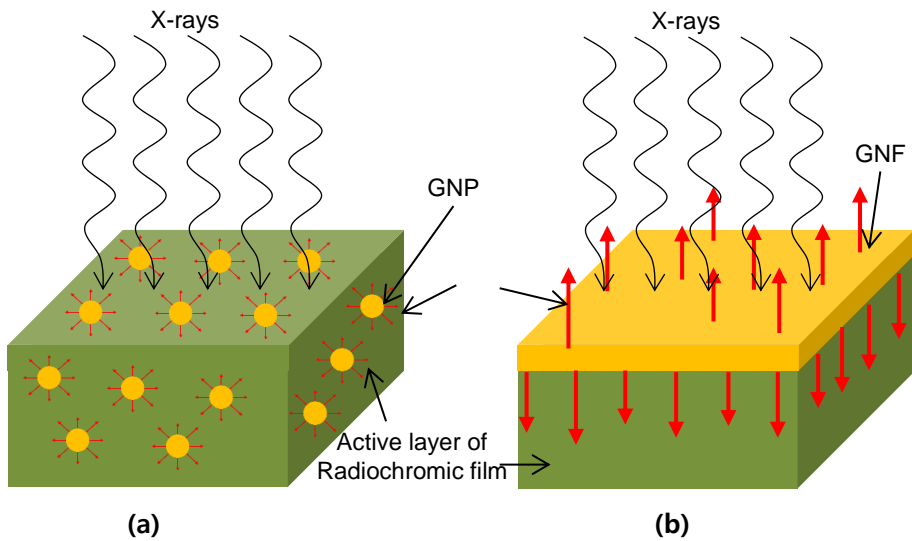


Figure 23. Schematic diagram of irradiation configurations for analytical calculation of dose enhancement (not scaled): (a) When gold nanoparticles (GNPs) of total mass m_{Au} are uniformly mixed with radiochromic film, low-energy electrons (LEEs) will deposit the whole energy into the radiochromic film. (b) The actual experimental setup in which the gold nanofilm (GNF) is attached to the active layer of radiochromic film. Polyester base of radiochromic film and PET substrate of GNF is not shown in the figure.

However, in the real experimental setup the GNF was attached on the top of the active layer (see Figure 23(b)). The cross-section per atom for photoelectric effect involves a complex calculation and also considers the angular distribution of emitted photoelectron. Heitler presented a simplified equation for K-shell electrons in an atom of atomic number Z:

$$\frac{d\sigma_{\tau}}{d\Omega_e} = 4\sqrt{2}r_e^2\alpha_0^4 \frac{Z^5}{\alpha^{7/2}} \frac{\sin^2\theta_e}{\left(1 - \frac{p_e}{m_0c^2\cos\theta_e}\right)^4} \quad (20)$$

where α_0 is the fine structure constant and p_e is the recoil electron momentum.⁸¹ In real experimental setup, a portion of the secondary electrons produced by X-rays will be emitted to the backward direction.⁸² MCNP6.1 (Monte Carlo N-Particle Transport Code Version 6.1) was used to calculate the fraction of backward, forward and self-absorbed electrons emitted from GNF.⁸³ In addition, continuous-slowing-down approximation (CSDA) ranges for electrons of 25.6, 48.3 and 1970 keV are 14.4 μm , 44 μm and 7088 μm , respectively. This means that the energy deposited by the secondary electrons from 50 kVp X-rays will be mostly confined within the first 14.4 μm of the active layer.⁴ This value is in agreement with the value of effective depth reported by Rakowski et al.³⁶ for 50 kVp X-rays. Therefore, in Eq.(20), m_{EBTXD} only corresponding to 14.4 μm thickness of the active layer should be considered for 50 kVp X-rays, while m_{EBTXD} of total thickness of the active layer (i.e., 25 μm) was used for 220 kVp and 6 MV FFF X-rays. The macroscopic DEF for the real experimental setup using GNF is given by:

$$\frac{1}{m_{\text{EBTXD}} + m_{\text{Au}}} \left(m_{\text{EBTXD}} + m_{\text{Au}} \left(\frac{f_{\text{Fwd}} \left(\frac{\mu_{\text{en}}}{\rho} \right)_{\text{E,Au}}}{\left(\frac{\mu_{\text{en}}}{\rho} \right)_{\text{E,EBTXD}}} \right) \right) \quad (21)$$

where f_{Fwd} is the fraction of electrons forward to the active layer.

2.2.6.2. Monte Carlo Simulations for Estimating f_{Fwd}

Parallel 25.6, 48.3 and 1970 keV photons were assumed to be incident on GNF in vacuum. The cut-off energy was set to 50 eV for both electron and photon. For the electron and photon transport, a physics library of eprdata12 was used. A single-event electron transport method was applied to LEEs of which energies were lower than 50 keV.⁸⁴ F1 tally (surface current) was used to detect the electrons crossing the upper surface (i.e., backward) and the lower surface (i.e., forward) of GNF. The number of particle histories was 1×10^7 for 25.6 and 48.3 keV X-rays and 4×10^9 for 1.97 MeV X-rays. The relative uncertainties (1σ) of the tallies were below 3.6%. The calculated fraction of forward electrons emitted from GNF was inserted into Eq. (20) to calculate the dose enhancement in the real experimental condition. In addition, Siegel et al. showed that the decline of lattice parameter of gold prepared in the form of a thin layer influences the density of gold.⁸⁵ They reported that the gold density increased with increasing the thickness of gold layer and then above 100 nm achieved the bulk value i.e., 19.3 g cm^{-3} . Their measured densities for the thicknesses of GNF were used to evaluate the mass composition of gold (see Table 12).

2.3. Results

2.3.1. Thickness Measurements of GNF

Figure 24 shows GNFs of nominal thicknesses 20, 30, 40, 50, and 100 nm that were prepared using a thermal evaporator on PET substrates. Coating thicknesses of GNFs were hardly distinguishable by their transparency. The Alpha-Step measured results are presented in Table 12. The thickness of GNF was estimated as a mean value of three different regions of gold slits. All the measured coating thicknesses of GNFs were thinner than the intended (or nominal) values. The deposition thickness depends upon the evaporation time, deposition rate and the type of substrate.

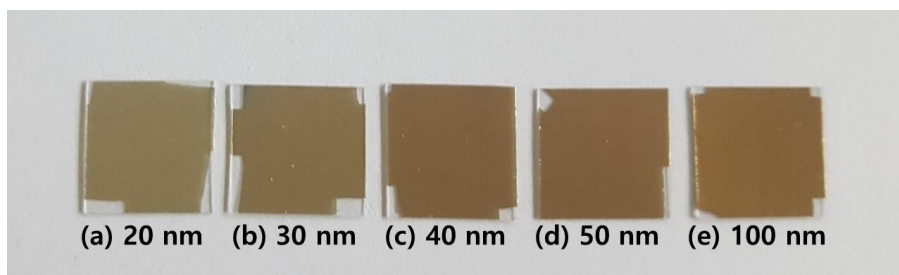


Figure 24. Gold nanofilms of various coating thicknesses on PET substrate. The thicknesses denoted here are nominal values.

Table 12. Coating thicknesses of Gold nanofilms (GNFs) measured by Alpha-Step and their respective densities⁸⁵ and masses. Fractions of electrons entering into the active layer of radiochromic film from GNF calculated by the MCNP 6.1 code are also included in the table.

Nominal thickness [nm]	Estimated thickness [nm]	Au density measured by Siegel <i>et al</i> 2017 [g·cm ⁻³]	Mass for ROI of 1 × 1 cm ² , m_{Au} [g]	Fraction of electrons entering into the active layer from GNF		
				50 kVp	220 kVp	6 MV FFF
20	19.7 ± 0.3	16.05	3.16 × 10 ⁻⁰⁵	0.542	0.594	0.861
30	29.5 ± 0.7	16.83	4.97 × 10 ⁻⁰⁵	0.546	0.609	0.885
40	38.5 ± 0.5	17.36	6.68 × 10 ⁻⁰⁵	0.544	0.606	0.898
50	47.7 ± 0.5	17.76	8.47 × 10 ⁻⁰⁵	0.543	0.610	0.908
100	90.9 ± 0.4	18.62	1.69 × 10 ⁻⁰⁴	0.537	0.599	0.931

2.3.2. Calibration Curves

The EBT-XD film calibration curves of optical flatbed scanner and Raman spectroscopy for 50 and 220 kVp and 6 MV FFF X-rays are shown in

Figure 25. The scanner responses of films (R) to doses (D) were fitted to Eqs. (22), (23), and (24) using Eq. (12) for the X-rays of three energies:

$$50 \text{ kV}_p: R(D) = 9641.2 + \frac{400639.8}{D + 9.8} \quad (22)$$

$$220 \text{ kV}_p: R(D) = 1123.1 + \frac{647023.3}{D + 13.6} \quad (23)$$

$$6 \text{ MV FFF}: R(D) = 3576.2 + \frac{546964.5}{D + 11.5}. \quad (24)$$

The Raman band height (Y) was exponentially increased with doses (D):

$$50 \text{ kV}_p: Y(D) = 42 - 29e^{-\frac{D}{1.9}} \quad (25)$$

$$220 \text{ kV}_p: Y(D) = 43 - 29e^{-\frac{D}{2.2}} \quad (26)$$

$$6 \text{ MV FFF}: Y(D) = 41 - 29e^{-\frac{D}{2.2}}. \quad (27)$$

The dynamic dose range of both methods was well suited within the calibrated range from 0 to 8.0 Gy. In addition, the three energy curves in

Figure 25(a) and (b) are nearly overlapping, showing the weak energy dependence of EBT-XD film. In

Figure 25, the relative standard deviations from the optical scanner and Raman spectrometer were within 1.1% and 10%, respectively.

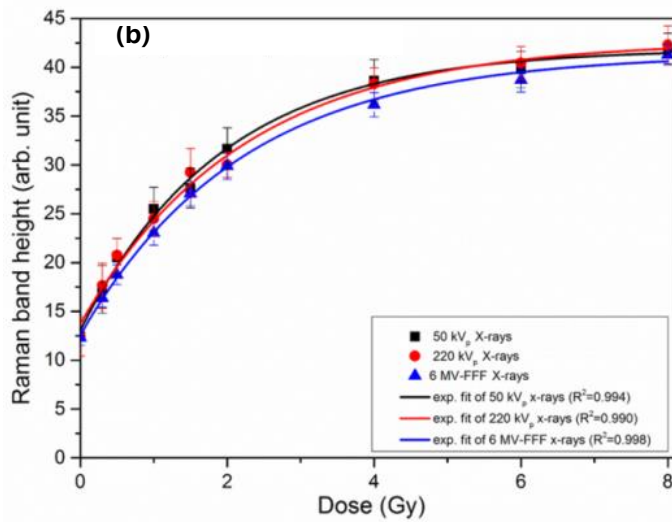
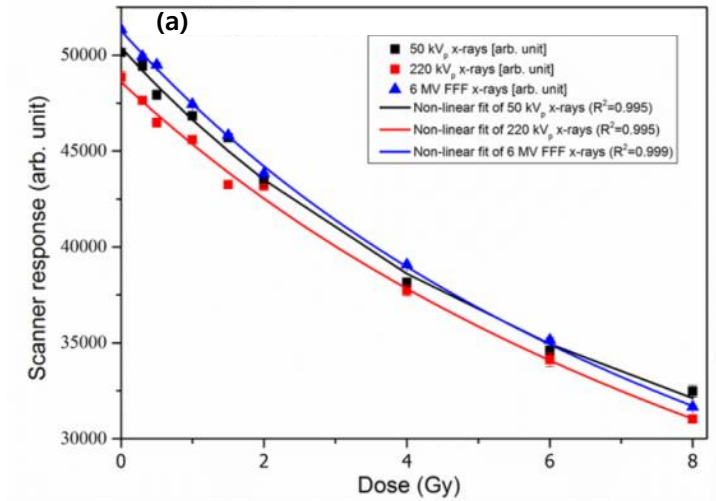


Figure 25. Dose calibration curves of (a) an optical scanner (error bars are the same size or smaller than the symbols) (b) and a Raman spectrometer for 50, 220 kV_p, and 6 MV FFF.

2.3.3. Dose Enhancement Factor

2.3.3.1. Experimental Measurement

Figure 26 shows the arrays of EBT-XD films aligned by delivered doses in order and thicknesses of gold-coating. Note that 0 thickness of gold-coating means a PET substrate alone. Figure 26(a) for 50 kVp and Figure 26(b) for 220 kVp show that the darkness of EBT-XD films (i.e., optical density) was increased with the thicknesses of gold-coating as well as the doses delivered to the films. However, Figure 26(c) for 6 MV FFF shows almost no change of the darkness along the y-axis (i.e., regardless of the thickness of gold-coating) and different optical densities developed only by delivered doses (along the x-axis).

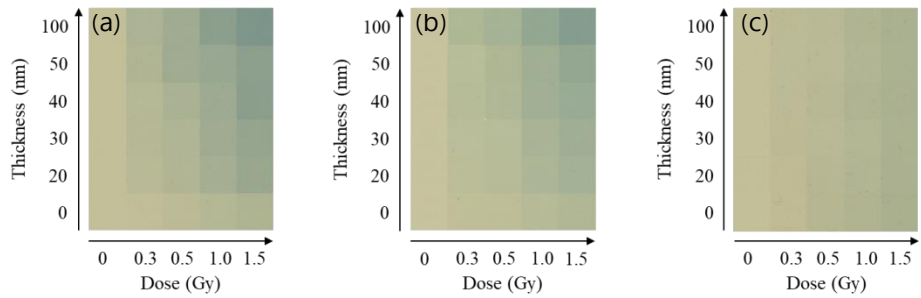


Figure 26. Arrays of unlaminated EBT-XD films after irradiation of 50, 220 kVp, and 6 MV FFF under GNF. X-axis indicates delivered doses 0, 0.3, 0.5, 1.0, and 1.5 Gy. Y-axis indicates the thicknesses of GNFs 0, 20, 30, 40, 50, and 100 nm. Darker color means that the EBT-XD film was more irradiated (along x-axis) or more dose-enhanced (along y-axis). The color became darker with increasing the thickness of GNF at (a) 50 kVp and (b) 220 kVp beams. However, the dose enhancement by change of thickness was hardly seen from the films irradiated by (c) 6 MV FFF beam.

The DEFs defined in Eq. (13) were calculated for the three X-ray energies and the five thicknesses of gold-coating from doses estimated by the two measurement methods and the analytical approach. The Chauvenet's criterion was applied to reject outlying data from the measurements.⁵⁹ Figure 27 shows variations of DEFs vs. thickness of gold-coating for the three X-ray energies. The dose enhancement factors determined from this procedure are also summarized in Table 13. The significant fluctuations in measured DEFs were observed in Figure 27. The non-uniform contact between GNF and the active layer of EBT-XD film at a micro-level might be one of the sources of this variability. In addition, the active layer of EBT-XD film was not uniformly coated in order of micrometer. Since the dose deposited by LEEs reached only a few tens nm depth of the active layer from GNF, such unevenness at the micrometer scale caused a large variation in readouts using both the optical scanner and Raman spectrometer. However, even with this variation, almost all the DEFs measured by the optical scanner lied within the error bars of Raman spectroscopy data.

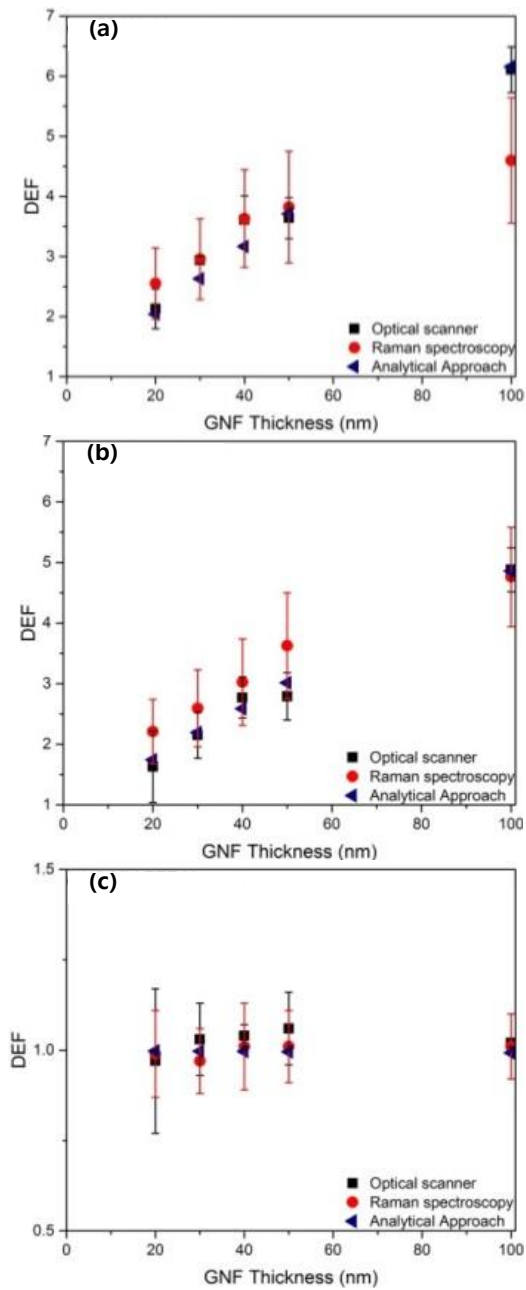


Figure 27. Comparison of DEF obtained from optical scanner, Raman spectroscopy, and analytical calculations for photon energies of (a) 50 kVp, (b) 220 kVp, and (c) 6 MV FFF beam. For low-energy X-rays DEF was an increasing function of GNF thickness, whereas enhancement was negligible for high-energy X-rays.

Table 13. List of DEFs for 50 and 220 kVp, and 6 MV FFF X-rays for GNFs of various thicknesses. These values were estimated by three different methods i.e. optical scanner, Raman spectrometer and analytical approach with an aid of MC simulations.

GNF Thickness	50 kVp			220 kVp			6 MV FFF		
	^a DEF _{OS}	^b DEF _{RS}	^c DEF _{AN}	DEF _{OS}	DEF _{RS}	DEF _{AN}	DEF _{OS}	DEF _{RS}	DEF _{AN}
20	2.13 (± 0.33)	2.55 (± 0.59)	2.04	1.63 (± 0.59)	2.21 (± 0.53)	1.74	0.97 (± 0.2)	0.99 (± 0.12)	0.998
30	2.94 (± 0.06)	2.96 (± 0.67)	2.63	2.15 (± 0.38)	2.59 (± 0.64)	2.19	1.03 (± 0.1)	0.97 (± 0.09)	0.997
40	3.61 (± 0.40)	3.63 (± 0.81)	3.17	2.77 (± 0.34)	3.03 (± 0.71)	2.59	1.04 (± 0.03)	1.01 (± 0.12)	0.996
50	3.64 (± 0.34)	3.82 (± 0.93)	3.71	2.79 (± 0.39)	3.63 (± 0.87)	3.01	1.06 (± 0.1)	1.01 (± 0.1)	0.996
100	6.11 (± 0.38)	4.60 (± 1.04)	6.16	4.88 (± 0.36)	4.76 (± 0.82)	4.86	1.02 (± 0.01)	1.01 (± 0.09)	0.993

^aDEF_{OS} measured by optical scanner response

^bDEF_{RS} measured by Raman spectrometer

^cDEF_{AN} Analytical calculations

2.3.3.2. Analytical Approach

The effective energies E_{eff} for 50 and 220 kVp, and 6 MV FFF photon beams were determined to be 25.6, 48.3 and 1970 keV, respectively. The mass energy absorption coefficient values corresponding to E_{eff} (National Institute of Standards and Technology, US)⁸⁶ were used in Eq. (15) to calculate the $(\mu_{\text{en}}/\rho)_{E_{\text{eff}},\text{EBTXD}}$ and $(\mu_{\text{en}}/\rho)_{E_{\text{eff}},\text{Au}}$. The masses of 14.4 and 25 μm -thick active layer of $1 \times 1 \text{ cm}^2$ RCF (m_{EBTXD}) were calculated as 1.94×10^{-3} and 3.38×10^{-3} g, respectively, whereas m_{Au} of various GNF thicknesses are presented in Table 12. The fraction of electrons entering into the RCF calculated by MC simulations are also presented in Table 12. Using data of Table 12 and the mass energy absorption coefficient values of RCF and gold inserted into Eq. (21), the macroscopic DEFs were calculated and presented in Table 13 and Figure 27. The dose enhancement increased by a few % by incorporating the thickness-variable gold densities of Table 12 as an alternative to the bulk value of $19.3 \text{ g}\cdot\text{cm}^{-3}$.

In general, for low-energy X-rays, both measured and analytical DEFs increased with increasing the thicknesses of GNF. However, the 6 MV FFF beam having a relative large amount of low-energy X-rays due to no filter failed to show any radioenhancement i.e., the experimental and analytical results shown in Figure 27 and Table 13 indicated that the dose enhancement by high-energy X-rays was negligible. The measured DEFs for 50 kVp were higher than the corresponding values for 220 kVp (Figure 27 (a) and (b)), regardless of the thicknesses of GNF, which was somewhat expected by the fact that photoelectric cross-sections steeply increase with decreasing photon

energy. The analytical estimation of DEFs for the three X-ray energies was in fair agreement within the error bars of measured data for all thicknesses of GNFs, except for the case of 100 nm-thick GNF and 50 kVp. The limitation of analytical approach at very low-energy X-rays will be further discussed below.

2.4. Discussion

Numerous authors reported on dose enhancement by metal NPs. Most of them were based on Monte Carlo simulations except for only a few on physical experimental observations and analytical calculations.^{22-28,72-77} In all these approaches, the authors used different concentrations and sizes of GNPs, different X-rays energies, and experimental scenarios. Therefore, the exact one-to-one comparison with ours was nearly impossible. Cho et al. (2009) predicted a DEF of 1.92 for 50 kVp X-rays beam at a tumor loaded uniformly with 18 mg Au/g.²⁶ Roeske et al. calculated the dose enhancement from NPs of different atomic numbers at various energies by using the mass energy absorption coefficients.⁷⁸ Regulla et al. and Rakowski et al. adopted the similar method to determine DEFs.^{36,87} Regulla et al. used a 150 μm -thick gold foil and thermally simulated exoelectron emission (TSEE) detector.⁸⁷ Their measured physical DEF was 100 within a range of 10 μm from the foil for 40 kVp X-rays. Rakowski et al. used GNPs and unlaminated EBT2 RCF to determine DEFs, as well as the MC method.³⁶ They showed a MC-calculated DEF of 19.31 within the first 0.25 μm -depth in water from about 23 nm thick GNP. However, their measured DEFs using EBT2 RCF showed strong energy dependence at low-energies.³⁶ Use of EBT-XD film in this study eliminated the disadvantage of dosimeter energy dependence, especially at low-energies. For 6 MV FFF X-rays, our measured and calculated DEFs were comparable to the previously published data (Figure 27 and Table 13). For high-energy X-rays, Cho et al examined a dose enhancement using BEAMnrc/DOSXYZnrc and assuming a concentration of 7 mg Au/g tumor

and found a DEF of 1.014.⁸⁸ Similarly, the DEF calculated by Roeske et al.⁷⁸ was 1.01.

The analytical calculations of DEF more or less underestimated the experimental results, especially at 50 kVp. As shown in Figure 23(a), in fact, the implementation of this analytical technique requires a uniform distribution and a high concentration of GNPs throughout the medium (EBT-XD dosimeter in our case). However, in our experiments GNF was in contact with the active layer of RCF. Under this condition, a fraction of the secondary electrons produced by X-rays should be backward due to their angular distribution as described in Figure 23(b).⁸² Greater the X-rays energy lesser is a fraction of backward secondary electrons. As explained by Roeske et al.,⁷⁸ the underestimation in the analytical calculations might be due to the exclusion of secondary photons produced by the interaction of the primary beam and also this approach could not model the backscatter produced at the interface of low and high Z materials.

2.5. Conclusions

The radiation dose enhancement due to interactions of low-energy 50 kVp, 220 kVp, and high-energy 6 MV X-rays with GNPs of 20 nm to 100 nm thickness was successfully quantified by measuring the variations in the optical density and the Raman spectra of RCF. The DEFs measured by both methods overlapped each other within their error bars. The fractions of electrons emitted from GNP and entering into RCF were calculated by MC simulations. The DEFs were analytically calculated by incorporating these fractions into a collisional kerma under CPE within the active layer of RCF. The calculated DEFs were also in agreement with the measured values. These experimental and analytical approaches developed in this study could quantitatively estimate radioenhancement of high-Z metallic NPs by low-energy X-rays, which has been an emerging interest in diagnostic and therapeutic applications of NPs. This work has a limitation in self-absorption and backscattering of low-energy electrons where the characteristics of GNP may differ from those of GNPs in tissues.

Discussion

The results of this work suggest that Raman spectroscopy can be used to determine absorbed dose with a high-spatial resolution by exploiting the idea that $C\equiv C$ and $C=C$ in RCFs increase with increasing dose due to polymerization of diacetylene monomer. The confocal Raman spectroscopy was used to acquire Raman spectra of laminated EBT3 and EBT-XD films. A depth for maximum dose was established using depth profiling while using metallurgical objective. The calibration curve with $C\equiv C$ band heights has dose non-uniformity $< 10\%$. The peak ratio method significantly improves the dose non-uniformity ($\pm 3\%$). Both EBT3 and EBT-XD films are suitable for micrometer resolution dosimetry. The micrometer resolution dosimetric characterization suggest that EBT3 film is preferred at low doses up to 2 Gy, whereas, EBT-XD is suitable for high doses. At low doses, Raman spectroscopy method is more sensitive compared to an optical scanner or densitometer. The micrometer resolution dosimetry by Raman mapping technique can be further improved by using a confocal microscope with immersion oil objective and using peak ratio method for the calibration curves.

The confocal Raman spectroscopy technique can be applied to find the dose enhancement caused by gold nanofilm. The analytical calculations of DEF more or less underestimated the experimental results, especially at 50 kVp. The implementation of this analytical technique requires a uniform distribution and a high concentration of GNPs throughout the medium. However, in our experiments, GNF was in contact with the active layer of RCF. Under this condition, a fraction of the secondary electrons produced by

X-rays should be backward due to their angular distribution. Greater the X-rays energy lesser is a fraction of backward secondary electrons. The underestimation in the analytical calculations might be due to the exclusion of secondary photons produced by the interaction of the primary beam and also this approach could not model the backscatter produced at the interface of low and high Z materials.

Conclusions and Future work

The Raman intensity for C=C and C≡C peaks increases with an increase in the amount of diacetylene polymerization due to an increase in dose. This study showed the potential of Raman spectroscopy as an alternative for absolute dosimetry verifications with a high-spatial resolution of a few μm , but these findings need to be further validated for the purpose of microdosimetry. Both EBT3 and EBT-XD films are suitable for micrometer resolution dosimetry by confocal Raman spectroscopy. Results of dosimetric characterization suggest that EBT3 films are suitable for low doses whereas, EBT-XD films are suitable for high dose applications. A micro-densitometer or microscope with an appropriate objective and light source can be used to achieve very high spatial resolution. However, reading out with Raman spectroscopy is advantageous in a sense that dose variation is less than 3% with peak ratio method when data is acquired with micrometer spatial resolution. Moreover, with Raman spectroscopy, we can analyze polymerization in colorless polymers. The document scanner or densitometer cannot analyze colorless films. Also, at low doses, the calibration curves obtained by Raman microscopy are more sensitive than document scanner or densitometer. Lastly, the dose enhancement due to low-energy X-ray interactions with GNP was quantitatively validated by measuring the variations in optical densities and Raman spectral shift on the RCFs. The experimental and analytical approaches developed in this study would be useful to quantitatively estimate radiosensitization of high-Z metallic nanoparticles by low-energy X-rays, which has been an emerging interest in

diagnostic and therapeutic applications of nanoparticles. This work has a limitation in self-absorption and backscattering of low-energy electrons where the characteristics of GNF may differ from those of GNPs in tissues

In future, we will characterize the RCF dosimeters by using oil immersion objective with confocal Raman microscopy and peak ratio methods. With Raman spectroscopy, we can observe the change in the molecular fingerprints of colorless monomer/polymers. We can exploit this concept in finding a new dosimeter material. Some potential dosimeters are listed in Appendix I. The selection criterion for the new dosimeter includes water equivalency, post-irradiation stability, dose sensitivity, energy and dose-rate dependency and the cost.

References

- ¹ R.B. King, S. J. McMahon, W. B. Hyland, S. Jain, K. T. Butterworth, K. M. Prise, A. R. Hounsell, and C. K. McGarry, "An overview of current practice in external beam radiation oncology with consideration to potential benefits and challenges for nanotechnology," *Cancer Nanotechnol.* **8**, (12 pp.) (2017).
- ² C. Elith, , S. E. Dempsey, N. Findlay, and H. M. W-Forward, "An introduction to the intensity-modulated radiation therapy (IMRT) techniques, tomotherapy, and VMAT," *J. Med. Imag. Radiat. Sci.* **42**, 37-43 (2011).
- ³ B. K. Chang, and R. D. Timmerman, "Stereotactic body radiation therapy: a comprehensive review," *Amer. J. Clin. Oncol.* **30**, 637-644 (2007).
- ⁴ F. H. Attix, *Introduction to radiological physics and radiation dosimetry*, (John Wiley and sons, Inc., Germany, 1986) p.501.
- ⁵ G. Cellere, and A. Paccagnella, "A review of ionizing radiation effects in floating gate memories," *IEEE Transactions on Device and Materials Reliability* **4**, 359-370 (2004).
- ⁶ AAPM Report No. 63, Radiochromic film dosimetry, 1998.
- ⁷ G. Heilemann, D. Georg, and A. Berg, in *Pushing the boundaries of spatial resolution in dosimetry using polymer gels and radiochromic films 2014: 8th International Conference on 3D Radiation Dosimetry (IC3DDose)*, Ystad, Sweden, 4-7 September 2014, *J. Phys.* **573**, IOP publishing, 012034 (5pp.) (2015).
- ⁸ M. Alqathami, A. Blencowe, U. J. Yeo, S. J. Doran, G Qiao, and M. Geso, "Novel multicompartement 3-dimensional radiochromic radiation dosimeters for nanoparticle-enhanced radiation therapy dosimetry," *Int. J. Radiat. Oncol. Biol. Phys.* **84**, e549-e555 (2012).
- ⁹ E. Bräuer-Krisch, A. Bravin, M. Lerch, A. Rosenfeld, J. Stepanek, M. Di Michiel, and J. A. Laissue. "MOSFET dosimetry for microbeam radiation therapy at the European Synchrotron Radiation Facility." *Med. Phys.* **30**, 583-589 (2003).
- ¹⁰ E. A. Siegbahn, E. Bräuer-Krisch, A. Bravin, H. Nettelbeck, M. L. F. Lerch, and A. B. Rosenfeld, "MOSFET dosimetry with high spatial resolution in intense synchrotron-generated x-ray microbeams," *Med. Phys.*, **36**, 1128-1137 (2009).
- ¹¹ M. D. Belley, I. N. Stanton, M. Hadsell, R. Ger, B. W. Langloss, J. Lu, O. Zhou, S. X. Chang, M. J. Therien, and T. T. Yoshizumi, "Fiber-optic

- detector for real time dosimetry of a micro-planar x-ray beam," *Med. Phys.* **42**, 1966-1972 (2015).
- ¹² J. Archer, E. Li, M. Petasecca, M. Lerch, A. Rosenfeld, and M Carolan, "High-resolution fiber-optic dosimeters for microbeam radiation therapy." *Med. Phys.* **44**, 1965-1968 (2017).
- ¹³ S. J. Doran, T. Brochard, J. Adamovics, N. Krstajic, E. B. Krisch, "An investigation of the potential of optical computed tomography for imaging of synchrotron-generated x-rays at high-spatial resolution," *Phys. Med. Biol.* **55**, 1531-1547 (2010).
- ¹⁴ J. C. Crosbie, I. Svalbe, S. M. Midgley, N. Yagi, P. A. W. Rogers, R. A. Lewis, "A method of dosimetry for synchrotron microbeam radiation therapy using radiochromic films of different sensitivity," *Phys. Med. Biol.* **53**, 6861-6877 (2008).
- ¹⁵ G. Massillon-JL, S.-T. Chiu-Tsao, I. Domingo-Muñoz, and M. F. Chan, "Energy dependence of the new Gafchromic EBT3 Film: Dose response curves for 50 kV, 6 and 15 MV X-Ray Beams," *Int. J. Med. Phys. Clin. Engin. and Radiat. Oncol.* **1**, 60-65 (2012).
- ¹⁶ J. A. Mirza, H. Park, S Park, and S Ye, "Use of radiochromic film as a high-spatial resolution dosimeter by Raman spectroscopy," *Med. Phys.* **43**, 4520-4528 (2016).
- ¹⁷ A. Z. Wang, and J. E. Tepper, "Nanotechnology in radiation oncology," *J. Clin. Oncol.* **32**, 2879-2885 (2014).
- ¹⁸ K. K. Jain, "Nanodiagnostics: application of nanotechnology in molecular diagnostics," *Expert Rev. Mol. Diag.* **3**, 153-161 (2003).
- ¹⁹ O. C. Farokhzad, and R. Langer. "Nanomedicine: developing smarter therapeutic and diagnostic modalities," *Adv. Drug Deliv. Rev.* **58**, 1456-1459 (2006).
- ²⁰ K. K. Jain, "Applications of nanobiotechnology in clinical diagnostics," *Clin. Chem.* **53**, 2002-2009 (2007).
- ²¹ S. Jung, W. Sung, and S-J Ye. "Pinhole X-ray fluorescence imaging of gadolinium and gold nanoparticles using polychromatic X-rays: a Monte Carlo study, *Int. J. Nanomed.* **12**, 5805-5817 (2017).
- ²² J. F. Hainfeld, D. N. Slatkin, and H. M. Smilowitz, "The use of gold nanoparticles to enhance radiotherapy in mice," *Phys. Med. Biol.* **49**, N309-N315 (2004).
- ²³ J. L. Robar, "Generation and modelling of megavoltage photon beams for contrast-enhanced radiation therapy," *Phys. Med. Biol.* **51**, 5487-5504 (2006).

- ²⁴ S. J. McMahon, M. H. Mendenhall, S. Jain, and F. Currell, "Radiotherapy in the presence of contrast agents: a general figure of merit and its application to gold nanoparticles," *Phys. Med. Biol.* **53**, 5635-5651 (2008).
- ²⁵ E. Brun, L. Sanche, and C. S-Roselli, "Parameters governing gold nanoparticle X-ray radiosensitization of DNA in solution," *Collo. Surf. B: Biointer.* **72**, 128-134 (2009).
- ²⁶ S. H. Cho, B. L. Jones, and S. Krishnan, "The dosimetric feasibility of gold nanoparticle-aided radiation therapy (GNRT) via brachytherapy using low-energy gamma-/x-ray sources," *Phys. Med. Biol.* **54**, 4889-4905 (2009).
- ²⁷ K. T. Butterworth, S. J. McMahon, F. J. Currell, and K. M. Prise, "Physical basis and biological mechanisms of gold nanoparticle radiosensitization," *Nanoscale* **4**, 4830-4838 (2012).
- ²⁸ W. Sung, S.-J. Ye, A. L. McNamara, S. J. McMahon, J. Hainfeld, J. Shin, H. M. Smilowitz, H. Paganetti, and Jan Schuemann, "Dependence of gold nanoparticle radiosensitization on cell geometry," *Nanoscale* **9**, 5843-5853 (2017).
- ²⁹ R. Delorme, F. Taupin, M. Flaender, J.-L. Ravanat, C. Champion, M. Agelou, and H. Elleaume, "Comparison of gadolinium nanoparticles and molecular contrast agents for radiation therapy-enhancement," *Med. Phys.* **44**, 5949-5960 (2017).
- ³⁰ R. Ravichandran, J. P. Binukumar, I. Al-Amri, and C. A. Davis, "Diamond detector in absorbed dose measurements in high-energy linear accelerator photon and electron beams." *J. App. Clin. Med. Phys.* **17**, 291-303 (2016).
- ³¹ Ashland Specialty Ingredients, 1005 US Highway 202/206, Bridgewater, NJ 08807.
- ³² M. Callens, W. Crijns, V. Simons, I. De Wolf, T. Depuydt, F. Maes, K. Haustermans, J. D'hooge, E. D'Agostino, M. Wevers, H. Pfeiffer, and K. Van Den Abeele, "A spectroscopic study of the chromatic properties of Gafchromic™ EBT3 films," *Med. Phys.* **43**, 1156–1166 (2016).
- ³³ D. Lewis, A. Micke, X. Yu, and M. F. Chan, "An efficient protocol for radiochromic film dosimetry combining calibration and measurement in a single scan," *Med. Phys.* **39**, 6339–6350 (2012).
- ³⁴ C. G. Soares, "Radiochromic film dosimetry," *J. Radiat. Meas.* **41**, S100–S116 (2007).
- ³⁵ S. Bartzsch, J. Lott, K. Welsch, E. Bräuer-Krisch, and U. Oelfke, "Micrometer-resolved film dosimetry using a microscope in microbeam radiation therapy," *Med. Phys.* **42**, 4069-4079 (2015).

- ³⁶ J. T. Rakowski, S. S. Laha, M. G. Snyder, M. G. Buczek, M. A. tucker, F. Liu, G. Mao, Y. Hillman, and G. Lawes, "Measurement of gold nanofilm dose enhancement using unlaminated radiochromic film," *Med. Phys.* **42**, 5937-5944 (2015).
- ³⁷ L. Rintoul, M. Lepage, and C. Baldock, "Radiation dose distribution in polymer gels by Raman Spectroscopy," *Appl. Spectroscopy* **57**, 51-57 (2003).
- ³⁸ Gafchromic™ EBT-XD Dosimetry film, Ashland Specialty Ingredients, Bridgewater, NJ 08807, 2015, available at http://www.gafchromic.com/documents/EBTXD_Specifications_Final.pdf.
- ³⁹ S. Devic, N. Tomic, and D. Lewis, "Reference radiochromic film dosimetry: review of technical aspects," *Phys. Med.* **32**, 541-556 (2016).
- ⁴⁰ D. F. Lewis. M. F. Chan, "Technical Note: On GAFChromic EBT-XD film and the lateral response artifact," *Med. Phys.* **43**, 643–649 (2016).
- ⁴¹ N. J. Overall, "Confocal Raman microscopy: common errors and artefacts." *Analyst* **135**, 2512-2522 (2010).
- ⁴² A. Palmer, A. Dimitriadis, A. Nisbet, and C. H. Clark, "Evaluation of Gafchromic EBT-XD film, with comparison to EBT3 film, and application in high dose radiotherapy verification," *Phys. med. biol.* **60**, 8741-8752 (2015).
- ⁴³ S. Saur and J. Fengen, "GafChromic EBT film dosimetry with flatbed CCDscanner: A novel background correction method and full dose uncertainty analysis," *Med. Phys.* **35**, 3094–3101 (2008).
- ⁴⁴ M. Abramoff, P. Magalhaes, and S. Ram, "Image processing with ImageJ," *Biophotonics Int.*, 11, 36-42 (2004)
- ⁴⁵ T. J. Collins, "ImageJ for microscopy," *Biotechniques* **43**, 25-30 (2007)
- ⁴⁶ V. C. Borca, M. Pasquino, G. Russo, P. Grosso, D. Cante, P. Sciacero, G. Girelli, M. Rosa La Porta, S. Tofani, "Dosimetric characterization and use of Gafchromic EBT3 film for IMRT dose verification," *J. Appl. Clin. Med. Phys.* **14**, 158-171 (2013).
- ⁴⁷ C.-M. Ma, C. W. Coffey, L. A. DeWerd, C. Liu, R. Nath, S. M. Seltzer, J. P. Seuntjens, "AAPM protocol for 40-300 kV x-ray beam dosimetry in radiotherapy and radiobiology," *Med Phys.* **28**, 863-893 (2011).
- ⁴⁸ M. Kamath, W. H. Kim, J. Kumar, S. Tripathy, K.N. Babu, and S. S. Talwar, "Kinetics of diacetylene polymerization: An FT Raman study, *Macromolecules*," *J. Am. Chem. Soc.* **26**, 5954-5958 (1993).
- ⁴⁹ E. Smith, and G. Dent, *Modern Raman spectroscopy-A practical approach* (John Wiley & sons Ltd., England, 2005) p. 3-4.

- ⁵⁰ T. Pradeep, *A text book of nanosciences and nanotechnology* (McGraw Hill, India, 2012) p. 846.
- ⁵¹ J. R. Ferraro, K. Nakamoto and C. W. Brown, *Introductory Raman Spectroscopy*, 2nd ed. (Elsevier, USA, 2003) p. 267, 274.
- ⁵² Princeton Instruments, "Confocal Raman microscopy General overview," Princeton instruments USA, available at <http://forum.sci.ccny.cuny.edu/cores/microscopy-imaging/raman/Confocal-raman-note.pdf>
- ⁵³ Dongwoo Optron, 102-8 Hoen-Daero, Gyeonggi-Do 1798, South Korea.
- ⁵⁴ R. L. Price, and W. G. Jerome, *Basic confocal microscopy* (Springer Science + Business Media, New York, 2011) p. 140.
- ⁵⁵ G. Gouadec, L. Bellot-Gurlet, D. Baron, and P. Colomban, "Raman mapping for the investigation of nano-phased materials," In *Raman imaging*, (Springer, Berlin, Heidelberg, 2012) pp. 85-118
- ⁵⁶ C. Raimondo, M. Alloisio, A. Demartini, C. Cuniberti, G. Dellepiane, S. A. Jadhav, G. Petrillo, E. Giorgetti, C. Gellini, and M. Muniz-Miranda, "Photopolymerization in water of diacetylenes chemisorbed onto noble metal nanoparticles: A spectroscopic study," *J. Raman Spectrosc.* **40**, 1831–1837 (2009).
- ⁵⁷ Christopher Homes C., G. Lawrence Carr, Ricardo PSM Lobo, Joseph D. LaVeigne, and David B. Tanner, "Silicon beam splitter for far-infrared and terahertz spectroscopy." *Applied optics* **46**, 7884-7888 (2007).
- ⁵⁸ Y. Tian, and K. S. Burch. "Automatic Spike Removal Algorithm for Raman Spectra." *Appl. Spectrosc.* **70**, 1861-1871 (2016).
- ⁵⁹ William Chauvenet, *A manual of spherical and practical astronomy* (J. B. Lippincott & Co, Philadelphia 1871).
- ⁶⁰ M. j. Pelletier, "Quantitative Analysis Using Raman Spectrometry," *Appl. Spectrosc.* **57**, 20A-42A (2003).
- ⁶¹ J. T. Bushberg, J. A. Seibert, E. M. Leidholdt, and J. M. Boone, "*The essential physics of medical imaging*," (Lippincott Williams & Wilkins Philadelphia, PA, 2012) p. 39-41.
- ⁶² J. Tessadori, M. Bisio¹, S. Martinoia¹, and M. Chiappalone¹, "Modular neuronal assemblies embodied in a closed-loop environment: toward future integration of brains and machines," *Fron. Neur. Circ.* **6**, 99 (16pp.) (2012).
- ⁶³ N. V. Klassena L. Zwan, and J Cygler, "GafChromic MD-55: Investigated as a precision dosimeter," *Med. Phys.* **24**, 1924-1934 (1997).
- ⁶⁴ C. G. Hammer, B. S. Rosen, J. S. Fagerstrom, W. S. Culberson and L. A. DeWeerd, "Experimental investigation of GafChromic[®] EBT3 intrinsic

- energy dependence with kilovoltage x-rays, ^{137}Cs , and ^{60}Co ,” *Med. Phys.* **45**, 448–59 (2017).
- ⁶⁵ J. G. H. Sutherland, D. W. O. Rogers, “Monte Carlo calculated absorbed-dose energy dependence of EBT and EBT2 film,” *Med Phys.* **37**, 1110–1116 (2010).
- ⁶⁶ H. Bekerat, S. Devic, F. DeBlois, K. Singh, A. Sarfehnia, J. Seuntjens, Shelley Shih, Xiang Yu, and D. Lewis, “Improving the energy response of external beam therapy (EBT) GafChromic™ dosimetry films at low energies (100 keV),” *Med Phys* **41**, 022101-1–022101-14 (2014).
- ⁶⁷ J. E. Villarreal-Barajas and R. F. Khan, “Energy response of EBT3 radiochromic films: Implications for dosimetry in kilovoltage range,” *J. Appl. Clin. Med. Phys.* **15**, 331–338 (2014).
- ⁶⁸ T. A. Brown, K. R. Hogstrom, D. Alvarez, K. L. Matthews II, K. Ham, J. P. Dugas, “Dose-response curve of EBT, EBT2, and EBT3 radiochromic films to synchrotron-produced monochromatic x-ray beams,” *Med Phys.* **39**, 7412–7417 (2012).
- ⁶⁹ L. Karsch, E. Beyreuther, T. Burris-Mog, S. Kraft, C. Richter, K. Zeil, and J. Pawelke, “Dose rate dependence for different dosimeters and detectors: TLD, OSL, EBT films, and diamond detectors,” *Med. Phys.* **39**, 2447–2455 (2012).
- ⁷⁰ T. Cheung, M. J. Butson, and P. K. Yu, “Post-irradiation colouration of Gafchromic EBT radiochromic film,” *Phys. Med. Biol.* **50**, N281–N285 (2005).
- ⁷¹ R. A. Freitas Jr, *Nanomedicine, volume I: Basic Capabilities*, (Landes Bioscience, Georgetown, TX, 1999) p. 247.
- ⁷² L. E. Taggart, S. J. McMahon, F. J. Currell, K. M. Prise, and Karl T. Butterworth. “The role of mitochondrial function in gold nanoparticle mediated radiosensitisation,” *Canc. Nanotechnol.* **5**, (12 pp.) (2014).
- ⁷³ H. Nikjoo, and L. Lindborg, “RBE of low energy electrons and photons,” *Phys. Med. Biol.* **55**, R65-R109 (2010).
- ⁷⁴ J. Schuemann, R. Berbeco, D. B. Chithrani, S. H. Cho, R. Kumar, S. J. McMahon, S. Sridhar, and S. Krishnan, “Roadmap to clinical use of gold nanoparticles for radiation sensitization,” *Int. J. Radiat. Oncol. Biol. Phys.* **94**, 189-205 (2016).
- ⁷⁵ B. L. Jones, S. Krishnan, and S. H. Cho, “Estimation of microscopic dose enhancement factor around gold nanoparticles by Monte Carlo calculations,” *Med. Phys.* **37**, 3809-3816 (2010).
- ⁷⁶ S. J. McMahon, K. T. Butterworth, C. K. McGarry, C. Trainor, J. M. O’Sullivan, A. R. Hounsell, and K. M. Prise, “A computational model of

- cellular response to modulated radiation fields,” *Int. J. Radiat. Oncol. Biol. Phys.* **84**, 250-256 (2012).
- ⁷⁷ Y. Lin, S. J. McMahon, H. Paganetti, and J. Schuemann, “Biological modeling of gold nanoparticle enhanced radiotherapy for proton therapy,” *Phys. Med. Biol.* **60**, 4149-4168 (2015).
- ⁷⁸ J. C. Roeske, L. Nuñez, M. Hoggarth, E. Labay, and R. R. Weichselbaum, “Characterization of the theoretical radiation dose enhancement from nanoparticles,” *Technol. Canc. Res. Treat.* **6**, 395-401 (2007).
- ⁷⁹ B. Palpant, B. Prével, J. Lermé, E. Cottancin, M. Pellarin, M. Treilleux, A. Perez, J. L. Vialle, and M. Broyer, “Optical properties of gold clusters in the size range 2–4 nm,” *Phys. Rev. B* **57**, 1963-1970 (1998).
- ⁸⁰ L. Menegotti, A. Delana, and A. Martignano, “Radiochromic film dosimetry with flatbed scanners: A fast and accurate method for dose calibration and uniformity correction with single film exposure,” *Med. Phys.* **35**, 3078–3085 (2008).
- ⁸¹ W. Heitler, *Quantum Theory of Radiation* (Oxford, 1955)
- ⁸² E. Acosta, X. Llovet, E. Coleoni, J. A. Riveros, and F. Salvat. “Monte Carlo simulation of x-ray emission by kilovolt electron bombardment,” *J. Appl. Phys.* **83**, 6038-6049 (1998).
- ⁸³ T. Goorley, M. James, T. Booth, F. Brown, J. Bull, L.J. Cox, J. Durkee, J. Elson, M. Fensin, R.A. Forster, J. Hendricks, H.G. Hughes, R. Johns, B. Kiedrowski, R. Martz, S. Mashnik, G. McKinney, D. Pelowitz, R. Prael, J. Sweezy, L. Waters, T. Wilcox, T. Zukaitis, “Initial MCNP6 release overview,” *Nucl. Technol.* **180**, 298-315 (2012).
- ⁸⁴ H.G. Hughes, “Recent developments in low-energy electron/photon transport for MCNP6,” *Prog. Nucl. Sci. Technol.* **4**, 454-458 (2014).
- ⁸⁵ J. Siegel, O. Lyutakov, V. Rybka, Z. Kolská, and V. Švorčík, “Properties of gold nanostructures sputtered on glass,” *Nanoscale Res. Lett.* **6**, (9 pp.) (2011).
- ⁸⁶ J. H. Hubbell, and S.M. Seltzer, *Tables of x-ray mass attenuation coefficients and mass energy-absorption coefficients from 1 keV to 20 MeV for elements Z = 1 to 92 and 48 additional substances of dosimetric interest*, Gaithersburg, MD: NIST Physical Measurement Laboratory; 1996. Available from: (<http://www.nist.gov/pml/data/xraycoef/index.cfm>).
- ⁸⁷ DF Regulla, L. B. Hieber, and M. Seidenbusch, “Physical and biological interface dose effects in tissue due to X-ray-induced release of secondary radiation from metallic gold surfaces,” *Radiat. Res.* **150**, 92-100 (1998).

- ⁸⁸ S. H. Cho, "Estimation of tumour dose enhancement due to gold nanoparticles during typical radiation treatments: a preliminary Monte Carlo study," *Phys. Med. Biol.* **50**, N163-N173 (2005).
- ⁸⁹ J-F. Blach, A. Daoudi, J-M. Buisine, and D. Bormann, "Raman mapping of polymer dispersed liquid crystal," *Vibrat. Spectr.* **39**, .31-36 (2005).
- ⁹⁰ Y. Liu, A. Qin, and B. Z. Tang, "Polymerizations based on triple-bond building blocks," *Prog. Poly. Sci.*, (47 pp) (2017).
- ⁹¹ Y. Hiejima, T. Kida, K. Takeda, T. Igarashi, and K Nitta, "Microscopic structural changes during photodegradation of low-density polyethylene detected by Raman spectroscopy," *Polym. Degrad. Stab.* **150** 67-72 (2018).
- ⁹² G. Y. Nikolaeva, E. A. Sagitova, K. A. Prokhorov, P. P. Pashinin, P. M. Nedorezova, A. N. Klyamkina, M. A. Guseva, and V. A. Gerasin, "Using Raman spectroscopy to determine the structure of copolymers and polymer blends," In *J. Phys.: Conference Series*, IOP Publishing **826**, p. 012002 (2017).
- ⁹³ K. A. Prokhorov, D. A. Aleksandrova, E. A. Sagitova, G. Yu Nikolaeva, T. V. Vlasova, P. P. Pashinin, C. A. Jones, and S. J. Shilton, "Raman Spectroscopy Evaluation of Polyvinylchloride Structure" In *J. Phys.: Conference Series*, IOP Publishing **691**, p. 012001(2016).
- ⁹⁴ I. Harada, M. Tasumi, H. Shirakawa, and S. Ikeda, "'Raman spectra of polyacetylene and highly conducting iodine-doped polyacetylene,'" *Chem. Lett.* **7**, 1411-1414 (1978).
- ⁹⁵ E. Rebollar, S. Pérez, M. Hernández, C. Domingo, M Martín, T. A. Ezquerro, J. P. García-Ruiz, and M. Castillejo, "Physicochemical modifications accompanying UV laser induced surface structures on poly (ethylene terephthalate) and their effect on adhesion of mesenchymal cells," *Physic. Chem. Chemi. Phys.* **16**, 17551-17559 (2014).
- ⁹⁶ H. W. Choi, H. J. Woo, W. Hong, J. K. Kim, S. K. Lee, and C. H. Eum, "Structural modification of poly (methyl methacrylate) by proton irradiation," *Appl. Surf. Sci.* **169**, 433-437 (2001).
- ⁹⁷ T. Fukushima, K. Takachi, and K. Tsuchihara, "Optically active poly (phenylacetylene) film: simultaneous change of color and helical structure," *Macromolecules* **39**, 3103-3105 (2006).
- ⁹⁸ J. P. Buisson, S. Lefrant, G. Louarn, J. Y. Mévellec, I. Orion, and H. Eckhardt, "Vibrational properties of poly (arylene vinylene) s." *Synth. Met.* **49**, 305-311 (1992).
- ⁹⁹ Wilson Jr, E. Bright, "The normal modes and frequencies of vibration of the regular plane hexagon model of the benzene molecule," *Physic. Rev.* **45**, 706 (1934).

- ¹⁰⁰ A. Chapiro, "Radiation induced polymerization," *Radiat. Phys. and Chem.* **14**, 101-116 (1979).
- ¹⁰¹ J. A. Sánchez-Márquez, R. Fuentes-Ramírez, I. Cano-Rodríguez, Z. Gamiño-Arroyo, E. Rubio-Rosas, J. M. Kenny, and N. Rescignano, "Membrane made of cellulose acetate with polyacrylic acid reinforced with carbon nanotubes and its applicability for chromium removal," *Int. J. Poly. Sci.* (2015).
- ¹⁰² M Little, H., and A. E. Martell, "Raman spectra of acetals." *J. Physic. Chem.* **53**, 472-482 (1949).
- ¹⁰³ V. Resta, G. Quarta, M. Lomascolo, L. Maruccio, and L. Calcagnile, "Raman and Photoluminescence spectroscopy of polycarbonate matrices irradiated with different energy 28Si^+ ions," *Vacuum* **116**, 82-89 (2015).
- ¹⁰⁴ M. Castriota, A. Fasanella, E. Cazzanelli, L. De Sio, R. Caputo, and C. Umeton, "In situ polarized micro-Raman investigation of periodic structures realized in liquid-crystalline composite materials," *Optics express* **19**, 10494-10500 (2011).

Appendix A.

Table A1. List of polymers as a potential candidate for micrometer resolution dosimetry by Raman spectroscopy.⁸⁹⁻¹⁰⁴

S. No.	Material	Raman peaks		
		Laser (nm)	Bond	Raman Peak (cm ⁻¹)
1	Polymer Dispersed Liquid Crystal (PDLC) Film	514.5	C≡N	2226
2	Polyethylene(PE)	532	C-C, CH ₂	1100, 1450
3	Polypropylene (PP)	532	Helical chain	809
4	Polyvinyl chloride (PVC), (VCM)	532	C-Cl, CH & CH ₂	500-800, 2800-3050
5	Polyacetylene (PA)	514.5	C=C	1485
6	polyethylene terephthalate (PET)	532	Ring mode 8a, C=O, Methylene group, aromatic C-H	1615, 1726, 2960, 3080
7	Polymethylmethacrylate (PMMA)	514.5, 632.8	CH ₃ , C-H bending, C=O, C-H stretching	816, 1460, 1720, 2800-3100
8	Polyphenylacetylenes (PPAs)	514.5	C-H, C-C	960,1340
9	Poly(arylene vinylene) (PPV)	514.5, 632.8	Benzene ring Wilson mode 9a and 8a, C=C	1171, 1583, 1625
10	Poly Acrylic acid	1064	C=C, C=O	1654, 1678
11	Acetal	514.5	C-C, C=O	953, 1795
12	Polycarbonate (PC)	514.5	C-O-C, Phenyl ring	1121,1611
13	Norland Optical Adhesive (NOA-61)	632.8	C=O, C=C, S-H	1746,1764, 1650, 2582

Abstract (in Korean)

목적: 높은 공간 분해능을 가지는 방사선량계에 대한 요구가 높아짐에 따라 방사선감광필름이 유력한 후보로 연구돼 왔지만, 평판 형광 스캐너와 같은 스캐닝 시스템에 의해 방사선감광필름의 효용성이 제한되었다. 근접방사선치료, 방사선 수술에서 높은 선량 기울기를 가진 영역의 방사선량을 측정하고, 싱크로트론 마이크로빔 방사선 치료에서 피크-대-밸리비를 측정하고, 금속 나노 입자에 의한 방사선량 증대 효과를 평가하기 위해서는 마이크로미터 해상도를 가지는 선량계가 필요하다. 본 연구에서는, 방사선감광필름을 이용한 높은 공간 분해능 측정의 대체 방법으로 현미경과 결합한 라만 분광법을 선택하였다. 또한 공 초점 라만 분광기를 사용하여 방사선감광필름에서 마이크로미터 공간 분해능으로 방사선량을 정량화할 가능성을 조사하였다. 마지막으로, 금 나노 입자와 광자의 상호작용으로 인한 방사선량 증대 효과를 정량적으로 측정하기 위해 이 기법을 적용하였다.

실험 방법: 상업용 방사선감광필름인 EBT3 그리고 EBT-XD는 50, 100, 200 및 300 kVp 및 6 MV 엑스선을 사용하여 알려진 선량으로 조사되었다. 0.3에서 30 Gy 의 선량이 본 연구에서 선택되었다. 공 초점 라만 분광기는 관심영역 (ROI) $100 \times 100 \mu\text{m}^2$ 에서 10

마이크로미터의 공간 분해능으로 라만 맵핑 기법을 적용하여 필름에 조사된 선량을 정량화 하는데 사용되었다. 두 종류의 방사선감광필름의 측정 가능한 공간 분해능, 임상적으로 유용한 선량 범위, 선량 감도, 선량 균일성, 방향 효과, 에너지 및 선량률 의존성 및 방사선 조사 후 필름의 안정성을 마이크로미터 분해능에서 특성화하였다.

개발된 기술은 방사선량 증대효과를 측정하기 위해 적용되었다. 폴리에틸렌 테레프탈레이트 (PET) 기판에 순금을 증발시켜 두께 20, 30, 50, 그리고 100 nm의 금 나노 필름 (GNFs)을 제조하였다. 금 나노 필름은 금 나노 입자의 결합체로 볼 수 있다. 방사선감광필름에 부착된 금 나노 필름은 50, 220 kVp 및 6 MV 평판 필터 프리 (FFF) 엑스레이를 사용하여 조사되었다. 방사선감광필름의 반응이 일어나는 층은 금 나노 필름과 접촉한 상태로, 코팅되어 있지 않은 PET 기판은 엑스레이 선원과 마주 본 상태로 조사하였다. 금 나노 필름이 있는 경우, 없는 경우, 두 경우에서 방사선 감광필름 내에 있는 반응이 일어나는 층의 방사선량을 평판 형광 스캐너와 공 초점 라만 분광기를 사용하여 측정하였다. 금 나노 필름이 있는 경우와 없는 경우 측정한 선량 비율을 방사선량 증대 인수 (DEF)로 정의하였다. 또한 방사선량 증대 인수의 분석적 계산을 위해 몬테카를로 전선모사 를

시행하였다.

실험 결과: 방사선 조사 후 부분적으로 이루어지는 디 아세틸렌의 중합으로 C=C 그리고 C≡C 두 개의 라만 피크가 각각 1447 cm⁻¹ 과 2060 cm⁻¹ 에서 관측되었다. 관심영역 (ROI) 100 × 100 μm² 에서 10 마이크로미터의 공간 분해능으로 측정된 데이터를 얻은 결과 선량 불 균일성은 10% 미만으로 관측되었다. EBT-XD 필름은 EBT3 필름에 비해 방사선량에 대한 민감도가 낮다. 2058 cm⁻¹의 C≡C 그리고 696 cm⁻¹ 에서의 C-C-C 밴드의 피크 비를 갖는 선량 반응도 또한 측정되었다. 피크 비율을 이용한 방법은 선량 불 균일성을 3% 정도까지 줄일 수 있었다. 두 종류의 방사선감광필름에서 모두 가로 (landscape) 방향이 세로 (Portrait)에 비해 C≡C 밴드 높이 반응도가 모든 선량에서 더 민감하게 관측되었다. 또한 EBT3, EBT-XD 두 필름 모두에서 낮은 에너지 의존성을 보였다. 두 필름 모두에서 선량률에 독립적이고 조사 24시간 후에 안정적인 반응을 보였다. EBT3 필름은 0에서 6 Gy의 낮은 선량에, EBT-XD 필름은 2에서 20 Gy의 높은 선량에 적합하였다.

50, 220 kVp 엑스선에서 20에서 100 나노미터 두께의 금 나노 필름에 대해 광학 스캐너로 측정된 방사선량 증대 인자 (DEF)는 각각 2.13 (± 0.33) 에서 6.11 (± 0.38) 그리고 1.63 (± 0.59) 에서

4.88 (± 0.36)로 측정되었다. 비슷하게 라만 분광장치를 이용하여 측정된 방사선량 증대인자는 50, 220 kVp 엑스선에서 각각 2.55 (± 0.59)에서 4.60 (± 1.04) 그리고 2.21 (± 0.53) 에서 4.76 (± 0.82)로 측정되었다. 몬테카를로 전산모사를 이용한 분석적인 방법으로 계산한 방사선량 증대효과는 금 나노 필름이 20에서 100 나노미터로 증가함에 따라 50 kVp에서 2.04에서 6.16, 220 kVp에서 1.74에서 4.86로 측정되었다. 하지만 분석적 계산, 실험에서 측정된 방법 모두에서 고 에너지 X 선에서는 방사선량 증대효과는 관찰되지 않았다. 분석적 계산을 통해 얻은 방사선량 증대 인자는 실험에서 얻은 값과 일치하는 경향을 보였다. 일반적으로 방사선량 증대효과는 금 나노 필름의 두께가 증가함에 따라 증가하였고, 엑스선 에너지를 증가함에 따라 감소하였다.

결론: 방사선량이 증가함에 따라 디 아세틸렌 중합량이 증가하면서, C=C 그리고 C≡C 라만 피크의 세기는 증가한다. 본 연구는 수 마이크로 미터의 높은 공간 분해능을 가진 절대 선량 측정의 검증의 대안으로 라만 분광법의 잠재성을 보여주었다. 본 연구에서 개발된 라만 선량측정법은 마이크로 선량 측정 목적을 위해서 추가적인 검증이 필요하다. EBT3, EBT-XD 두 필름 모두 공 초점 라만 분광장치로 볼 때 마이크로 미터 해상도 선량 측정에 적합하다. 선량 측정 결과 EBT3 필름은 0에서 6 Gy의 저 선량의

범위에서, EBT-XD 필름은 2에서 20 Gy의 고 선량의 범위에서 적합했다. 마지막으로 금 나노 입자와 저 에너지 엑스선의 상호작용으로 인한 방사선량 증대 효과는 광학 밀도의 변화와 방사선감광필름의 라만 스펙트럼 위치 변화를 측정함으로써 정량적으로 검증되었다. 본 연구에서 개발된 실험적, 분석적 접근법은 나노 입자의 진단 및 치료 응용분야에서 관심을 불러일으킨 저 에너지 엑스선에 의한 높은 원자번호를 가진 금속 나노입자의 방사선 민감도를 정량적으로 평가하는데 유용할 것이다. 본 연구는 금 나노 필름의 특성이 조직의 금 나노 입자 특성과 저 에너지 전자의 자기 흡수 및 후방 산란의 차이를 가질 수 있다는 점에서 한계를 가진다. 이후, 라만 분광장치 선량계는 두 개의 피크 비율 방법을 사용하여 높은 선량 균일성을 얻기 위해 확장 될 것이다. 라만 선량 측정을 위한 잠재적인 후보로 새로운 고분자 물질에 대한 연구가 진행될 필요가 있다.

주요어: 마이크로 미터 해상도 선량계, 라만 분광법, 공 초점, 고 공간 해상도, 방사선감광필름, 금 나노 입자 그리고 필름, 방사선량 증대효과

학 번: 2014-31483